Li *et al. Microstructures* **2025**, *5*, 2025080
DOI: 10.20517/microstructures.2024.207

Microstructures

Review

Open Access

MXene-based hydrovoltaic electricity generators and their coupling with other energy harvesting systems

Shengyou Li[1,#], Jinjie Liu[2,#], Kaiying Zhao[1], HoYeon Kim[1], EunAe Shin[1,3], Gwanho Kim[1], Guangtao Zan[1,4]

[1]Department of Materials Science and Engineering, Yonsei University, Seoul 03722, Republic of Korea.
[2]Department of Applied Physics, The Hong Kong Polytechnic University, Hong Kong 100872, China.
[3]Korea Packaging Center, Korea Institute of Industrial Technology, Bucheon 14449, Republic of Korea.
[4]School of Chemical Science and Engineering, Tongji University, Shanghai 200092, China.
[#]Authors contributed equally.

Correspondence to: Prof. Guangtao Zan, Department of Materials Science and Engineering, Yonsei University, 50 Yonsei-ro Seodaemun-gu, Seoul 03722, Republic of Korea. E-mail: gtzan@yonsei.ac.kr

How to cite this article: Li, S.; Liu, J.; Zhao, K.; Kim, H.; Shin, E.; Kim, G.; Zan, G. MXene-based hydrovoltaic electricity generators and their coupling with other energy harvesting systems. *Microstructures* **2025**, *5*, 2025080. https://dx.doi.org/10.20517/microstructures.2024.207

Received: 31 Dec 2024 **First Decision:** 22 Jan 2025 **Revised:** 16 Feb 2025 **Accepted:** 20 Feb 2025 **Published:** 4 Jul 2025

Academic Editor: Jungho Ryu **Copy Editor:** Fangling Lan **Production Editor:** Fangling Lan

Abstract

MXenes, a class of two-dimensional transition metal carbides and nitrides, have garnered significant attention for their unique properties, making them promising candidates for next-generation energy harvesting technologies. Among these, emerging MXene-based hydrovoltaic electricity generators (HEGs), including moisture electricity generators, evaporation electricity generators, reverse electrodialysis electricity generators, and droplet electricity generators, have demonstrated exceptional performance in converting energy in environmental water such as moisture, water, wave, and droplets into electricity. Additionally, the synergistic coupling of MXene HEGs with other energy harvesting systems, such as triboelectric nanogenerators and thermoelectric generators, offers new avenues for enhancing power generation performance and expanding application scenarios. This review systematically examines the structures and properties of MXenes, their application in various HEGs, and the recent advancements in their integration with other energy harvesting systems. Furthermore, we discuss the challenges and future opportunities for MXene-based devices in multifunctional energy harvesting platforms.

Keywords: MXene, hydrovoltaic electricity generators, energy harvesting, moisture electricity generator, evaporation electricity generator, coupling systems

INTRODUCTION

With the intensification of the global energy crisis and environmental pollution, the development and utilization of sustainable clean energy have become imperative[1-11]. To date, various energy harvesting devices have been developed to capture and utilize green energy from nature. These include photovoltaic (PV) cells for harnessing solar energy, thermoelectric generators (TEGs) for harvesting temperature gradient energy, triboelectric nanogenerators (TENGs) for converting mechanical energy, microbial electrochemical systems (MESs) that employ microbial metabolism to generate bioelectricity or produce value-added chemicals, and, more recently, hydrovoltaic electricity generators (HEGs) that generate electricity through direct interactions between different forms of water and nanomaterials[12-16]. However, devices such as PV cells, TEGs, TENGs and MESs often face limitations related to time or space. For instance, PVs struggle to operate during nighttime or cloudy conditions, while TEGs are typically constrained to environments with significant temperature differentials, such as industrial waste heat or automobile exhaust. In contrast, HEGs stand out due to their ability to utilize water in diverse forms through different mechanisms, enabling them to generate electricity without being restricted by time or location[17-21]. This makes HEGs a promising candidate for long-term and versatile energy harvesting applications.

HEGs, named in analogy to PV, combine "hydro" referring to water, and "voltaic" denoting the generation of electricity. As their name implies, they specifically refer to "the generation of electricity through direct interactions between nanomaterials and various forms of water". Water exists in multiple forms, including moisture, flowing water, waves, droplets, and water with varying salinity, all of which can be utilized for electricity generation. To date, four representative types of HEGs have been developed to exploit these different forms of water: moisture electricity generators (MEGs), evaporation electricity generators (EEGs), electrodialysis electricity generators (REGs), and droplet electricity generators (DEGs) [Figure 1]. The theoretical and experimental foundations of hydrovoltaic phenomena can be traced back over a century. For instance, the observation of streaming potential in 1859 laid the groundwork for modern EEGs. Similarly, the concept of reverse electrodialysis (RED), proposed in 1945, provided the theoretical basis for REGs. Although the principles behind HEGs have a long history, progress in this field remained slow until the development of nanomaterials and nanotechnology in the 21st century, which spurred rapid advancements and broader interest. The term "hydrovoltaic" was only introduced in 2018 to unify and describe devices capable of directly generating electricity from water in various forms. This term has since gained widespread recognition. Unlike traditional large-scale hydroelectric power plants, which rely on gravitational potential energy and classical electrodynamics to indirectly generate electricity through electromagnetic effects, HEGs are typically small, lightweight, and potentially wearable, making them highly promising for diverse applications. However, their current power generation efficiency remains low, significantly limiting their further development and practical implementation.

To enhance the power generation performance of HEG devices, various active materials have been explored in device design, including inorganic nanomaterials such as graphene oxides (GO), MXene, and SiO_2, natural biomaterials such as cellulose and proteins, and polyelectrolytes such as Poly(styrene sulfonic acid) (PSSA) and Poly(diallyldimethylammonium chloride) (PDDA)[22]. Among these, two-dimensional (2D) MXene materials have emerged as particularly promising for HEGs due to their unique advantages, including tunable chemical compositions, modifiable surface structures, easily adjustable porous nanochannels, large specific surface area, and excellent conductivity[23-25]. The ultrathin nanosheets of MXene, with their atomic-level thickness, expose all their surfaces, significantly increasing the interaction area with water molecules. Their adjustable chemical compositions and surface structures enhance interfacial interactions with water, improving charge separation capabilities. Additionally, their controllable

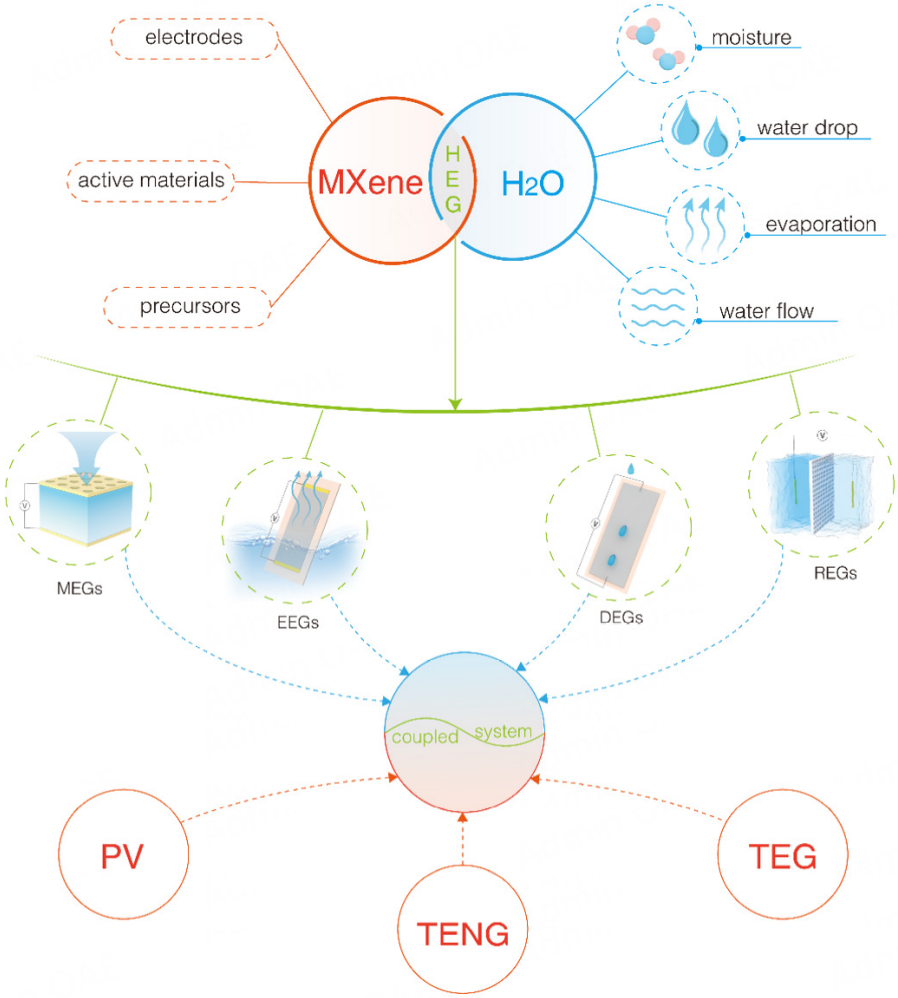

Figure 1. The overall outline of the review.

assembly enables the creation of more nanochannels, accelerating ion diffusion. Furthermore, their relatively high conductivity facilitates stronger interactions between electrons and ions. These characteristics make 2D MXene highly sensitive to water molecules, with enhanced water-solid phase interactions that improve energy conversion efficiency and significantly boost the power generation performance of HEGs.

Moreover, coupling HEGs with other energy harvesting technologies in the design of MXene-based systems can further enhance the utilization of environmental energy for better power generation [Figure 1]. This approach not only complements and significantly improves power generation performance but also expands the scope of potential functional applications. For instance, integrating HEGs and PVs can substantially increase the efficiency of environmental energy utilization. Combining HEGs with TENGs holds promise for applications in self-powered multimodal sensors and personalized healthcare. Meanwhile, coupling HEGs with TEGs could enable dual-energy recovery from waste heat and exhaust gases in industrial plants and automobiles. These synergistic strategies provide exciting opportunities for versatile and efficient energy harvesting systems.

From the above analysis, MXene materials exhibit tremendous potential for applications in HEG devices. However, a comprehensive review of MXene in this field is currently lacking. Therefore, this review aims to summarize the latest progress of MXene in the domain of HEGs [Figure 1]. We will begin by discussing the structural characteristics and physicochemical properties of MXene. Following this, we will explore its applications in four key areas: MEGs, EEGs, DEGs, and REGs. For each category, we will delve into the power generation mechanisms, the roles of MXene, and emphasize the structure-function relationships within HEG devices. Subsequently, we will highlight recent advancements in coupling MXene-based HEGs with other energy harvesting systems. Finally, the review will conclude with a summary of the key insights and a forward-looking discussion on promising future research directions.

OVERVIEW OF MXENES

Structures of MXenes

MXene was first reported in 2011 by Professors Naguib *et al.*, and their collaborators at Drexel University[26]. The earliest identified MXene material is $Ti_3C_2T_x$, which remains the most widely used due to its high electrical conductivity and well-established synthesis methods[27-30]. MXenes represent a family of 2D layered materials composed of transition metal carbides, nitrides, and carbonitrides. Their general chemical formula is $M_{n+1}X_nT_x$, where n ranges from 1 to 4, M denotes an early transition metal such as Ti, Zr, V, Nb, or Mo, X represents either carbon (C) or nitrogen (N), and T_x refers to surface terminations. These terminations can include oxygen (O), hydroxyl (OH), amines, halogens, chalcogens, and, more recently, antimony (Sb) and phosphorus (P) [Figure 2A and B].

Given the wide range of transition metals, carbon and nitrogen options, four archetypical MXene structures, and various monatomic surface terminations, over a thousand stoichiometric compositions are theoretically possible. To date, more than 50 distinct MXenes have been reported. When considering solid solutions with varying element ratios and diverse surface terminations, which significantly influence MXene properties, the total number of experimentally synthesized MXenes likely approaches a hundred. The diverse composition provides a rich library of materials for exploring solid-liquid-gas interfacial interactions and constructing various HEG structures.

Preparation of MXenes

The synthesis methods of MXenes are generally classified into two major categories: the top-down method and the bottom-up method [Figure 2C][30,31]. The top-down approach, which is the most widely used for MXene synthesis, involves selectively etching the A-layer elements from MAX phase materials to produce MXene nanosheets with rich surface chemistry. This section focuses on this widely adopted method. In contrast, the bottom-up approach has emerged more recently and is primarily based on chemical vapor deposition (CVD). However, research and practical applications of this method remain limited. Therefore, this section will provide a brief overview of the top-down synthesis of MXenes.

The top-down synthesis of MXenes typically involves three key steps: (1) Preparation of MAX Phase Precursors. The synthesis of MAX phase materials is a prerequisite for the top-down method. MAX phases are layered materials with the general structure $M_{n+1}AX_n$, where n = 1-4, M is a transition metal, A is a group IIIA or IVA metal (e.g., aluminum or silicon), and X is carbon or nitrogen. MAX phases are commonly synthesized through solid-state reactions; (2) Selective Etching of A-layer Atoms. This step is the core of the top-down process, where the A-layer elements are selectively removed to produce weakly bonded MXene multilayers. Two primary etching routes are commonly employed: Fluoride ion-containing acids: These acids selectively etch the A-layers, resulting in multilayered MXene particles or in situ delaminated 2D flakes. Molten salts: MAX phases are etched in molten salts, typically yielding multilayered MXene

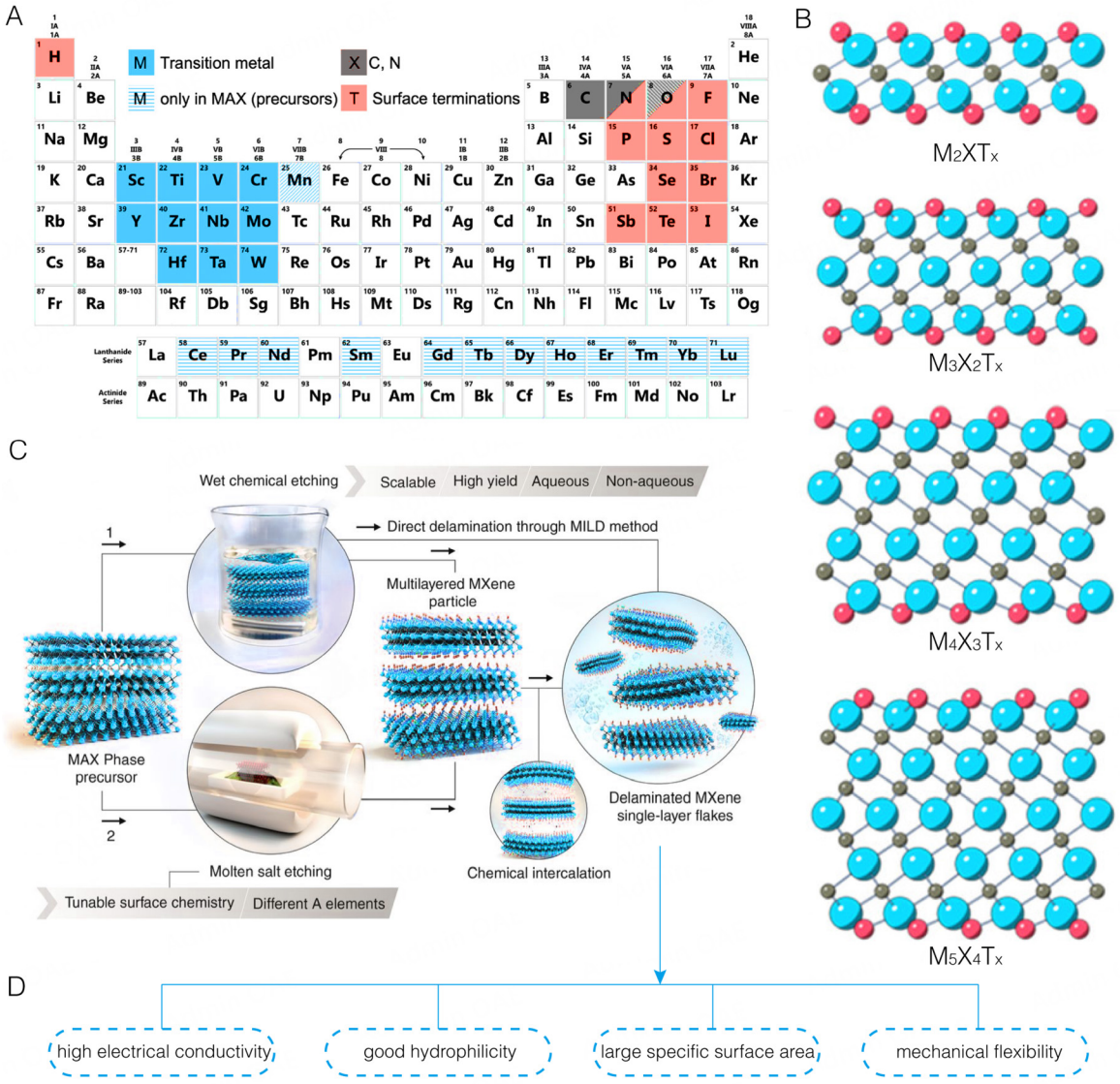

Figure 2. Structures and properties of MXene. (A) Elements constituting MXene. Reproduced with the permission from Ref.[28] Copyright 2022 Springer Nature. (B) Atomic structure model of MXene. Reproduced with the permission from Ref.[29] Copyright © 2023 American Chemical Society. (C) Schematic of MXene synthesis. Reproduced with the permission from Ref.[30] Copyright © 2021 The American Association for the Advancement of Science. (D) Properties of MXene.

particles[32]; (3) Delamination of $M_{n+1}X_nT_x$ Multilayers into Single Sheets. A common approach is the intercalation of molecules or ions to expand the interlayer spacing and weaken interflake interactions, followed by agitation or sonication to exfoliate the layers into a stable colloidal solution of single- to few-layered MXenes. These obtained single-layered or few-layered structures lay the foundation for further modification and the assembly of HEGs with diverse architectures.

Properties of MXenes

MXene, with its unique advantages in electrical conductivity, hydrophilicity, specific surface area, and mechanical properties, demonstrates significant potential for applications in HEG materials and devices. Additionally, its distinctive photothermal properties open new possibilities for enhancing HEG performance and integrating with other energy harvesting systems [Figure 2D][33,34].

In terms of electrical conductivity, MXene exhibits exceptionally high conductivity as high as 20,000 S cm^{-1}, primarily attributed to the d-electron orbitals of its transition metal elements, which confer metallic-like conductive properties[35,36]. Moreover, its conductivity can be tuned by modifying its surface terminations. These terminations influence the density of states (DOS) and shift the Fermi level, enabling MXene to transition from a conductor to a semiconductor[30,37]. This tunability enhances the versatility of MXene, making it not only suitable as an electrode material but also as an active material in HEGs[38].

Secondly, MXene exhibits strong hydrophilicity, due to its surface polar groups, such as -OH, -O, and -F. These functional groups not only enhance MXene's hydrophilicity but also ensure its stable dispersion in aqueous solutions. This greatly improves its processability, enabling the fabrication of various materials with different dimensions, including fibers, films, and aerogels, thereby broadening its application scenarios[39]. More importantly, these surface functional groups also impart a high zeta potential (approximately -30 mV) to MXene, facilitating strong interactions with water molecules. This enhances the adsorption of water molecules on its surface and promotes efficient charge separation. Additionally, when MXene membranes are used in REGs, their charged surfaces endow them with excellent ion selectivity for high-performance osmotic energy harvesting.

Additionally, the single-layered or few-layered MXene units provide an abundance of exposed surface area, while their controllable assembly prevents layer stacking and generates hierarchical pore structures with a large specific surface area. Such structure significantly increases the number and efficiency of interaction sites between MXene and water molecules, thereby enhancing charge generation capacity. Moreover, the hierarchical channels within the structure facilitate the rapid diffusion of water molecules and ions, significantly improving charge transfer efficiency. As a result, these characteristics enable MXene to excel in HEG applications.

Furthermore, MXene possesses exceptional mechanical flexibility. Thanks to its graphene-like 2D layered structure, MXene can withstand bending, stretching, and other deformations without losing its functional properties. This flexibility makes it particularly well-suited for use in wearable devices or integration onto flexible substrates, allowing it to adapt to a wide range of application scenarios[40-42].

RESEARCH PROGRESS OF MXENE-BASED HEGS

MXene-based MEGs

Mechanism of MEGs

Moisture, the gaseous form of water, is ubiquitous and abundant on Earth, comprising approximately one-tenth of the total water content of all the planet's lakes. MEGs can adsorb moisture from the air and convert it into electrical energy, garnering significant interest over the past decade. In 2015, Zhao *et al.* pioneered the development of a GO-based MEG and investigated the underlying mechanism of moisture-to-electricity conversion[43]. Since then, extensive advancements have been made in the design and development of MEG devices, incorporating diverse active materials (e.g., inorganic materials, organic materials, organic-inorganic hybrid materials), device dimensions (e.g., fibers, films, hydrogels, and aerogels), and device structures (e.g., sandwich-type, bilayer-type, and asymmetric-type configurations).

MEGs operate based on ion concentration gradient diffusion, a widely accepted mechanism. To create such a gradient, two primary strategies are commonly employed: one involves directly constructing a functional group gradient within the power-generating material, while the other relies on directional water infiltration into the material. The latter approach has garnered broader research attention due to its simplicity in both methodology and structure and the wide availability of compatible materials. In this review, we will

illustrate the power generation mechanism using the most prevalent design, specifically sandwich-structured MEG devices [Figure 3A][44]. These devices typically feature a top electrode that is either a mesh or partially covers the middle active material, while the bottom electrode completely covers the active material [Figure 3A]. To achieve asymmetric moisture adsorption, the bottom and sides of the device are generally encapsulated, leaving only the top exposed to air for moisture adsorption. A sandwich-structured MEG, utilizing sulfonated polyacrylamide (PAM) hydrogel as the electricity-generating functional layer, is presented as a representative example to elucidate the detailed power generation process [Figure 3B], which can be distinctly divided into three sequential steps[45]: (1) Moisture adsorption. The excellent water absorption of hydrogel, due to the introduction of LiCl, allows a significant number of water molecules to adsorb onto its upper surface. These water molecules then permeate into the hydrogel's interior through swelling; (2) Ion dissociation. The sulfonic acid groups on the polymer chains exhibit strong ionization in the presence of water, leading to the dissociation of abundant H^+ ions. Due to the asymmetric moisture adsorption structure, H^+ ions predominantly accumulate on the top surface of the hydrogel, creating a vertical ion gradient; and (3) Ion migration and charge separation. The accumulated H^+ ions begin to diffuse automatically toward the bottom side of the hydrogel driven by the ion concentration difference. When an external circuit is connected, the internal ion diffusion generates an electric current, enabling the conversion of moisture into electrical energy. Notably, in this system, Li^+ ions play a crucial role by breaking the hydrogen bonds within the polymer chains and creating additional ion transport pathways via the Hofmeister effect, thereby accelerating the diffusion of H^+ ions to achieve better output performance.

For MEG devices, the number of dissociated ions generated by the active material and their diffusion efficiency within the porous network of the active material play a pivotal role in determining power generation performance. MXene, with its abundant oxygen-containing functional groups, can dissociate a significant number of mobile hydrogen ions upon contact with water molecules, serving as effective charge carriers for MEG devices. Moreover, the assembly of MXene can generate a highly porous structure that facilitates ion diffusion, significantly enhancing its power generation performance. These unique properties position MXene as a highly promising active material for MEG applications. Table 1 provides a detailed summary of the MEG properties of recently reported MXene-based MEGs and highlights the specific roles MXene plays in their operation.

Advances in MXene-based MEGs

To date, MXene has been utilized in MEG devices in multiple roles - not only as an active electricity-generating material but also as a precursor for deriving other highly active MEG materials. Additionally, it has been employed as a conductive additive to reduce internal resistance. To enhance the power generation performance of MXene-based MEGs, various device architectures have been developed, including simple sandwich structures, bilayer structures with a water-absorbing layer serving as a reservoir, and asymmetric structures featuring dual-ion gradients. Based on the unique characteristics of these architectures, diverse applications have been explored, with representative examples including power supply units, self-powered sensors, and actuators.

In a simple sandwich-structured MEG device, MXene sheets can serve directly as an active material for dissociating mobile H^+ ions to establish ionic gradients[46,49,50]. For example, Luo *et al.* reported a fabric-based MEG device comprising MXene-coated cotton (MC) fabrics and SnO/SnO_2-grown carbonized silk (SCS) fabrics [Figure 3C][46]. The device configuration featured an active Al electrode as the top electrode, with SCS fabrics serving as the bottom electrode. MC fabrics acted as the active layer responsible for building proton gradient. In addition, the negatively charged pores in the SCS layer facilitate ion selectivity and migration, while the active Al electrode generates more mobile Al^{3+} ions through chemical reactions. These factors result in the Al-MC-SCS MEG exhibiting a high open-circuit voltage (V_{oc}) of 0.934 V and a high short-circuit current (I_{sc}) of 0.434 mA [Figure 3D].

Li *et al. Microstructures* **2025**, *5*, 2025080 | https://dx.doi.org/10.20517/microstructures.2024.207

Table 1. Summary of recent reported MXene-based MEGs

Functional layers	Electrodes	Roles of MXene	Area (cm^{-2})	Stabilized V_{oc} (V)	Stabilized J_{sc} ($\mu A\ cm^{-2}$)	Lasting time	Maximum power density ($\mu W\ cm^{-2}$)	RH (%)	Temperature	Ref.
MXene cotton + SnO/SnO_2/carbonized silk	Al/Carbon	Proton dissociation	1.5	0.932	289	20,000 s	26.66	/	Room temperature	[46]
MoS_2/MXene Cotton + (MoS_2)-carbonized silks	Al/Carbon	Proton dissociation	4	1.16	170	25,000 s	32.26	/	Room temperature	[49]
CMC/MXene/LiCl aerogel	Steel/Steel	Proton dissociation	/	0.12	/	/	/	77	25 °C	[57]
Cellulose/MXene/PSSA film	Ag/Ag	Proton dissociation	1	0.3 (peak)	1.2 (peak)	100 s	81.2 uW/cm^{-3}	80	20 °C	[55]
CMC/MXene/Al^{3+} composite film	Cu/Cu	Proton dissociation	14	0.055	/	1,000 s unchanged (V_{oc})	/	90	Room temperature	[56]
CNF/MXene/CMC composite film	Cu/Cu	Proton dissociation	4.5	0.167	/	/	/	/	Room temperature	[58]
Nb_2CT_x/sodium alginate composite film	Cu-Ni/Cu-Ni	Proton dissociation	0.5	0.5	1.6	6 h unchanged (V_{oc})	0.5	91.5	Room temperature	[50]
PAM hydrogel + MXene aerogel	Cu/Cu	Proton dissociation	1	0.6	1,160 (peak)	500 h unchanged (V_{oc})	24.8	20	20 °C	[47]
PAM organic-ionic hydrogel + MXene sponge	Ag/Ag	Proton dissociation	4	0.3	450	30 min unchanged (V_{oc})	9.15	20	20 °C	[51]
PANI-PVA-MXene films	CNT/CNT	Proton dissociation	2	0.4	1,800 (peak)	300 s unchanged (V_{oc})	3	/	Room temperature	[48]
TiO_2@Ti_3C_2 film	Ni/CNT	Precursor of TiO_2	1	0.8	50	1,000 s unchanged (V_{oc})	/	90	Room temperature	[52]
MXene-CNCs-tamarind gum-PAM hydrogel	Cu/Cu	Conductivity	5	0.164	/	/	/	/	Room temperature	[53]
Agar/PDACl/MXene + Agar/PSSNa/MXene organohydrogel	Cu/Cu	Conductivity	0.785	0.068	/	30 min unchanged (V_{oc})	/	99	25 °C	[54]

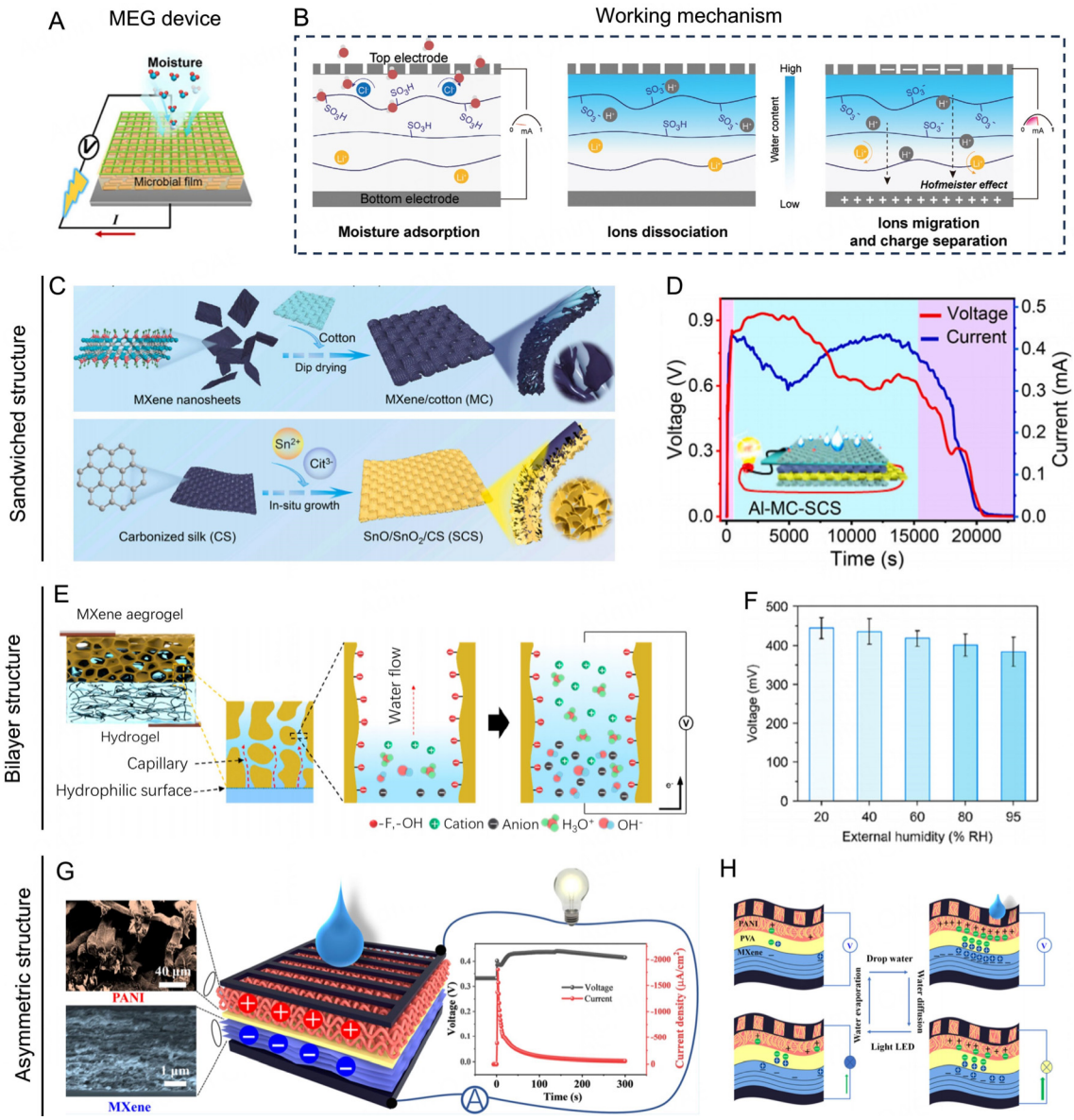

Figure 3. Working mechanism of MEGs and typical MEGs using MXenes as active materials. (A) Typical sandwich-type device structure of MEG. Reproduced with the permission from Ref.[44] Copyright © 2023 Elsevier Ltd. (B) Schematic illustration showing the power-generation processes in a representative MEG. Reproduced with the permission from Ref.[45] Copyright © 2023 Wiley-VCH. (C) Schematic illustration of the preparation of MC and SCS fabrics. (D) V_{oc} and I_{sc} curves of Al-MC-SCS MEG tested over 20,000 s. Reproduced with the permission from Ref.[46] Copyright © 2023 Elsevier Ltd. (E and F) Schematic illustration showing the power-generation process of the MXene-based bilayer MEG (E), and corresponding V_{oc} output under different RHs (F). Reproduced with the permission from Ref.[47] Copyright © 2023 American Chemical Society. (G and H) Schematic illustration and performance of MXene-based asymmetric MEG (G), and corresponding working mechanism (H). Reproduced with the permission from Ref.[48] Copyright © 2021 American Chemical Society.

Although the simple sandwiched MEGs can achieve exceptionally high V_{oc} and I_{sc} outputs, their performance is highly susceptible to interference from relative humidity (RH) and demonstrates minimal electrical output under low-humidity conditions. To overcome this limitation, bilayer structure is introduced, which includes a water-absorbing layer that acts as a reservoir to mitigate the impact of external humidity fluctuations and a functional layer containing MXene to enable efficient charge separation and ion diffusion. Zhao *et al.* developed a humidity-resistant bilayer MEG device comprising MXene aerogel and a

PAM ionic hydrogel [Figure 3E][47]. In this design, the MXene aerogel serves as the electricity-generating layer, while the underlying PAM hydrogel acts as a water reservoir. As water from the PAM ionic hydrogel infiltrates MXene channels, hydrolysis of oxygen-containing groups renders them negatively charged. This selective transport allows only cations to pass through, leading to charge accumulation at the top and bottom of the MXene aerogel, forming an internal electric field [Figure 3E]. Based on this bilayer structure, the MEG maintains a stable voltage across a wide RH range [Figure 3F]. Similarly, Kim *et al.* introduced a bilayer moisture-resistant MEG comprising a MXene-coated sponge and PAM hydrogel[51]. Due to the excellent flexibility and stretchability of the sponge and hydrogel, along with their strong interfacial bonding, the MEG maintains a stable V_{oc} output under various mechanical deformations.

Besides, fabricating asymmetric structures with dual-ion gradients has also proven to be an effective strategy for enhancing the performance of MXene-based MEGs. For example, Li *et al.* reported an asymmetric MEG consisting of negatively charged MXene (NCM) and positively charged polyaniline (PANI) membranes [Figure 3G][48]. At the PANI interface, OH^- anions diffuse toward the polyvinyl alcohol (PVA) film, while the NCM surface releases H^+ cations, migrating in the same direction [Figure 3H]. The potential difference between PANI and MXene restricts ion diffusion, creating a quasi-static equilibrium that stabilizes the voltage output.

Additionally, MXene can serve as a precursor for synthesizing TiO_2 with MEG activity. For instance, Liu *et al.* reported a high-performance MXene-derived TiO_2 film obtained through HCl treatment for sandwiched MEG, which was used as the electricity-generating active material[52]. The MXene-derived TiO_2 MEG outputs a V_{oc} of 0.8 V and an I_{sc} of 50 μA at 90% RH. The authors used molecular dynamics (MD) simulations to demonstrate the adsorption and splitting of water molecules on the TiO_2 (001) surface [Figure 4A]. Density functional theory (DFT) simulations further confirmed the enhancement of the work function by water adsorption and its reduction by HCl treatment. Based on experimental and simulation data, the authors summarized the triple role of water molecules and detailed the MEG power generation process [Figure 4B].

MXene can also function as a conductive additive to reduce the internal resistance of the device, thereby enhancing its responsiveness to humidity[53,54]. He *et al.* developed a multifunctional conductive double-network (DN) hydrogel for wearable strain sensors and MEGs[53]. This DN hydrogel consists of ionically crosslinked tamarind gum networks and covalently crosslinked PAM networks [Figure 4C]. MXene/CNC composites were incorporated as conductive additives, as CNCs effectively disperse MXene nanosheets. The resistance of the DN hydrogel was sensitive to various external stimuli. Under humidity stimulation, the MEG generates a peak V_{oc} output of 164 mV.

Applications of MXene-based MEGs

Benefiting from the material modifications and device design, MXene-based MEGs exhibit diverse application potential [Figure 5]. MXene-based MEGs can serve as power sources for driving small electronic devices, such as calculators, alarm clocks, and light-emitting diode (LED) lamps, with their output performance enhanced by connecting multiple units in series and parallel [Figure 5A-C][47]. Additionally, due to the high moisture absorption and sensitivity of MXene-based MEG devices to external humidity, they have been explored for potential applications in self-powered sensors[47], actuators[47,56,58], and water-collection devices[57].

When an MEG device is attached to the body, it can monitor the degree of finger flexion in real time [Figure 5D][47]. Moreover, the I_{sc} of MXene-based MEGs is highly sensitive to changes in external RHs,

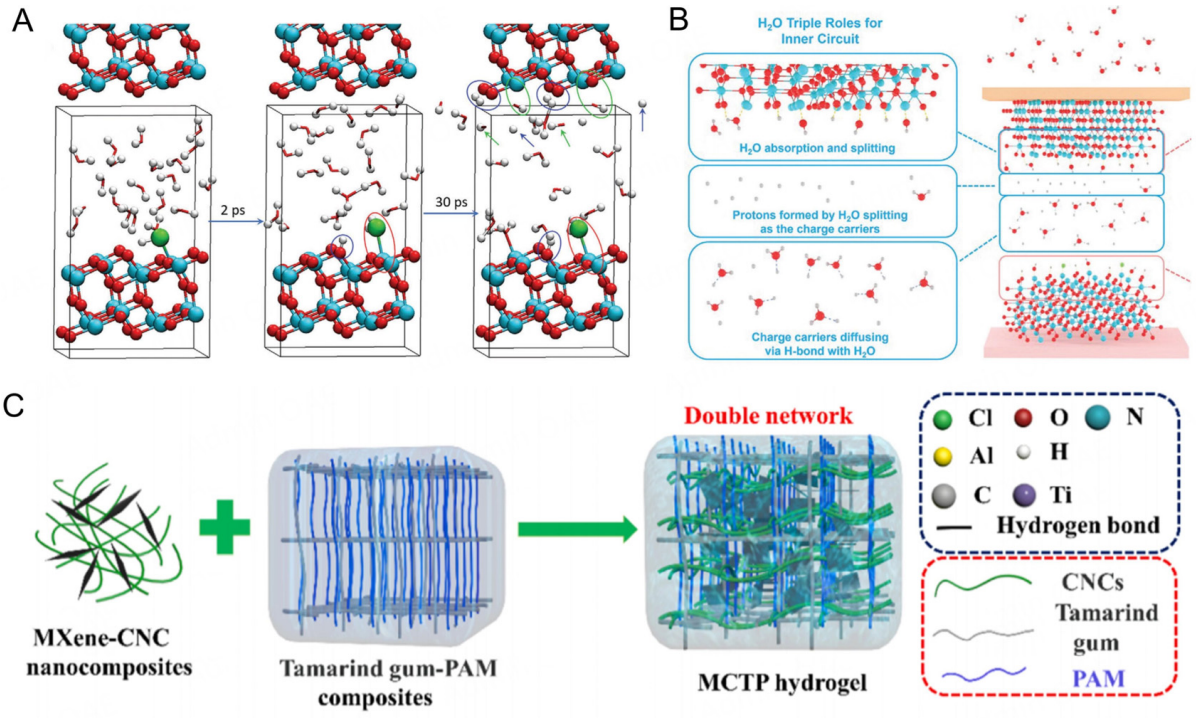

Figure 4. MXene as precursor and conductive additive for MEGs. (A) MD calculations displaying the process of water molecules absorption on (101) crystal planes of TiO_2. (B) Schematic illustration showing triple roles of water molecules during power generation. Reproduced with the permission of Ref.[52] Copyright © 2024 Wiley-VCH. (C) Schematic illustration of the double-network structure of MCTP hydrogel. Reproduced with the permission of Ref.[53] Copyright © 2021 Elsevier B.V.

enabling dynamic monitoring of the RH status in the surrounding environment. As shown in Figure 5E and F, MXene-based MEGs can detect respiratory patterns before and after exercise, along with water loss from the skin (e.g., fingertips)[8]. This capability offers a novel self-powered sensing approach for wearable healthcare applications.

For moisture-driven actuators, Li *et al.* developed a multifunctional MXene/cellulose/Polystyrene sulfonic acid membrane (MCPM) capable of both moist-electric generation and humidity-driven actuation [Figure 5G][55]. Under asymmetric moisture stimuli, protons dissociated from the Polystyrene sulfonic acid (PSSA) layer create a proton gradient from the top to the bottom of the membrane. Simultaneously, the MCPM can fold into various angles under differing humidity levels, enabling its use as a self-powered actuator. Specifically, the MCPM can fold from 28° to 130° as the RHs change from 20% to 97%. To further investigate the role of MXene nanosheets in moisture-driven actuation, Wei *et al.* fabricated a carboxymethyl cellulose (CMC)/MXene membrane via Al^{3+} ionic crosslinking[56]. When the CMC/MXene membrane absorbs moisture on one side, it bends toward the dry side. This occurs due to hydrophilic groups in CMC and MXene, which facilitate water absorption and transport, increasing *d*-spacing on the more exposed bottom side. The resulting stress gradient induces bending, while desorption upon humidity removal restores the original shape of the membrane [Figure 5H].

MEGs are typically accompanied by moisture adsorption during the power generation process, wherein gaseous water is converted into liquid water stored within the active material. This process opens up a novel application field for MEG devices: the integration of power generation and water harvesting to achieve hydropower cogeneration[59-64]. Cai *et al.* demonstrated this potential with a vertically channeled

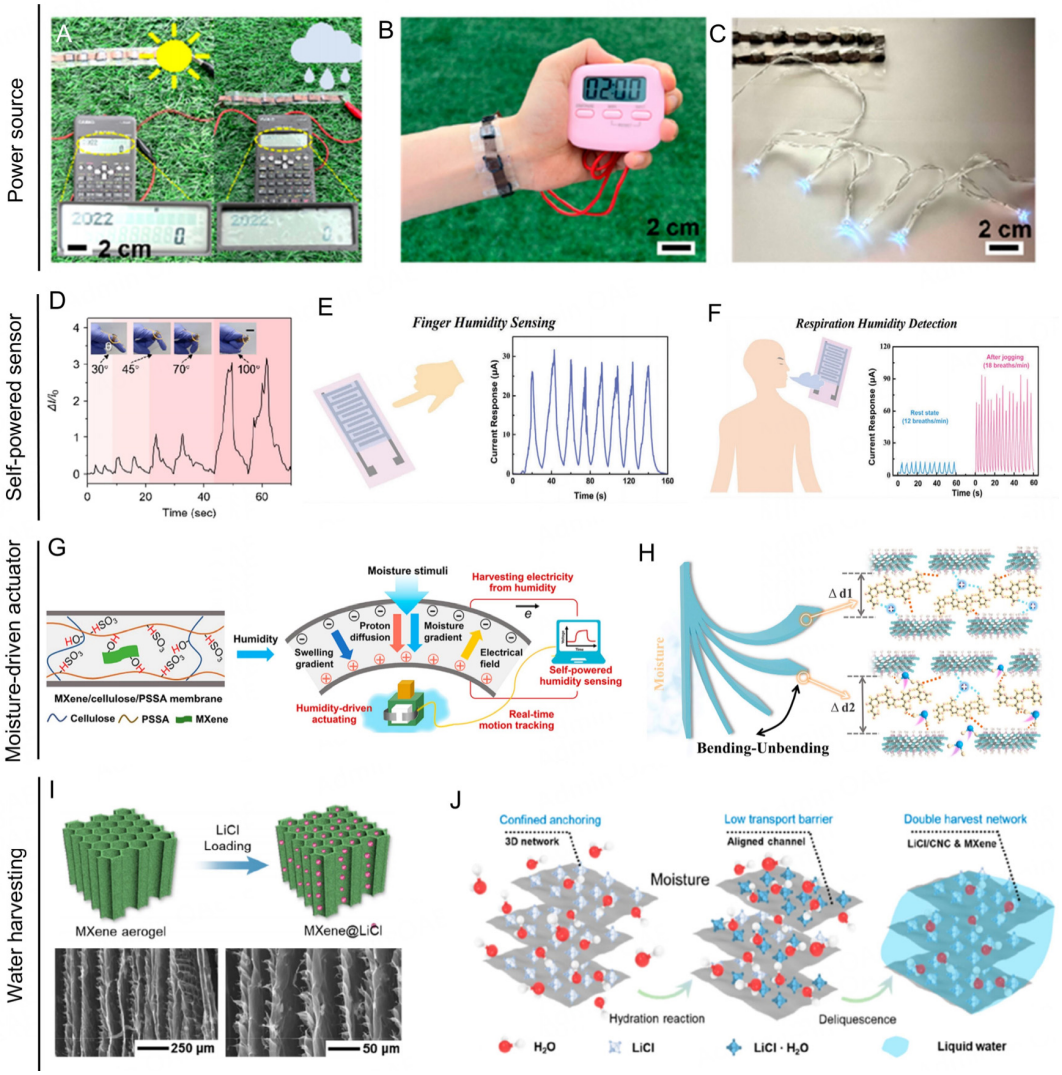

Figure 5. Diverse applications of MXene-based MEGs. (A-C) Flexible and wearable power source to drive small electronic devices, including (A) calculator, (B) clock and (C) LED lights. (D-F) Self-powered sensors for healthcare monitoring, including (D) wearable strain sensing, Reproduced with the permission of Ref.[47] Copyright © 2023 American Chemical Society. (E) finger humidity sensing, and (F) respiration humidity detection. Reproduced with the permission of Ref.[52] Copyright © 2024 Wiley-VCH. (G) Schematic illustration of the structure of MCPM film and corresponding humidity-driven actuating. Reproduced with the permission of Ref.[55] Copyright © 2021 American Chemical Society. (H) The bending-unbending mechanism of CMC/MXene/Al^{3+} composite film under asymmetric RHs. Reproduced with the permission of Ref.[56] Copyright © 2022 Elsevier B.V. (I) Schematic illustration of MXene@LiCl aerogel. (J) Schematic illustration of water absorption mechanisms. Reproduced with the permission of Ref.[57] Copyright © 2024 American Chemical Society.

MXene@LiCl aerogel designed for water harvesting [Figure 5I][57]. LiCl was uniformly dispersed within the aerogel walls without disrupting its structure, significantly enhancing water adsorption. At 90% RH, it achieved a water collection efficiency of 3.12 g g^{-1}. This improvement stems from LiCl hydration, forming LiCl·H_2O, which lowers the water adsorption barrier and facilitates migration. Combined with hydrophilicity of MXene, this dual mechanism enables exceptional water collection [Figure 5J]. Besides water harvesting, the MXene@LiCl aerogel serves as an active MEG material, generating a V_{oc} of 0.12 V at 77% RH. This dual functionality enables hydropower cogeneration, highlighting its multifunctional potential.

In summary, MXene materials are mainly used as active layers in MEG devices. To enhance power generation performance and stability, various strategies have been employed, including introducing negatively charged ion channels, constructing asymmetric structures, designing bilayer systems for separate water collection and power generation, and electrode modulation. Nevertheless, the performance of current MXene-based MEGs remains significantly limited compared to those utilizing other materials. Most of the existing strategies focus on device design, while research involving the chemical modification of MXene itself is relatively scarce. Therefore, future studies should place greater emphasis on this aspect, aiming to enhance MEG performance through more fundamental material-level design. Additionally, long-term stability assessments of MEG devices, spanning several weeks or months, remain rare, despite their critical importance for practical applications. This issue warrants substantial attention and further investigation.

MXene-based EEG

Mechanism of EEG

Water evaporation is a ubiquitous and continuous natural phenomenon, where the phase transition from liquid to gas occurs spontaneously by absorbing ambient thermal energy. It was not until 2017 that Xue *et al.* introduced EEGs, demonstrating that the energy changes associated with water evaporation could be effectively harvested for electricity generation. This pioneering work sparked rapid interest and development in the field[65].

We will use this EEG device as an example to elaborate on its structural design and power generation mechanism. In this device, a rectangular carbon black (CB) film was deposited onto an insulating substrate, with multi-walled carbon nanotubes (MWCNTs) positioned at both ends of the CB film as electrodes. The entire device was partially immersed in bulk water [Figure 6A][65]. On the water-contacting side, liquid water infiltrated the CB film through capillary action, allowing water molecules to flow through the porous network formed between CB flakes. This natural evaporation process ensured a continuous capillary flow, enabling long-term operation with a sustained output of a V_{oc} of up to 1 V and a I_{sc} of 150 nA.

Studies have shown that the working mechanism of EEGs is closely related to streaming potential. As early as 1859, Quincke experimentally observed that when an electrolyte flows through a narrow channel under pressure, a potential difference - known as the streaming potential - is generated. The power generation mechanism of EEGs is highly analogous to this phenomenon. In EEGs, continuous water evaporation and capillary action drive water flow through the porous channels formed by the stacked nanomaterials. Due to surface functional groups or electrostatic interactions, these nanomaterial-based porous channels are typically surface-charged, leading to the formation of an electric double layer (EDL) at the water-channel interface [Figure 6B][44]. Within the diffuse layer of the EDL, a large number of counterions accumulate, while co-ions are nearly absent. As water evaporates, counterions undergo directional migration, inducing an electric current in the external circuit.

Similar to carbon-based materials, MXene nanosheets feature surfaces rich in oxygen-containing functional groups, enabling the formation of EDLs when water molecules flow across them[66]. This makes MXene an excellent candidate for EEG applications. Table 2 summarizes the performance metrics of MXene-based EEG devices reported in recent years and highlights the critical role played by MXene in their operation.

Advances in MXene-based EEG

Owing to the sensitive response of Mxene to water molecules, the constructed EEGs are not only capable of generating electricity when immersed in conventional liquid water but can also directly harvest energy from water droplets and sweat. This capability allows MXene-based EEGs to overcome the dependency on large

Table 2. Summary of reported MXene-based EEGs

Functional layers	Electrodes	Roles of MXene	Area (cm^{-2})	Stabilized V_{oc} (V)	Stabilized J_{sc} ($\mu A\ cm^{-2}$)	Lasting time	Maximum power density ($\mu W\ cm^{-2}$)	Conditions	Temperature (°C)	Ref.
$Ti_3C_2T_x$/polyaniline-coated fabric	Cu/Cu	EDL effect	3.5	0.69 (peak)	2,157 (peak)	2,500 s	371	1 M NaCl	/	[67]
MXene-coated fabric	Zn/Zn	EDL effect	2	0.687 (peak)	1,500 (peak)	240 s	684	Sweat	/	[68]
GO/CNT/$Ti_3C_2T_X$-coated fabric	Ni/Ni	EDL effect	30	0.25	17.3	600 s unchanged (V_{oc} and I_{sc})	2.08	3.5 wt% NaCl	Room temperature	[66]
PVA/MXene film	Pt/Pt	Proton dissociation	1.5	0.4	2.67	300 min (V_{oc})	/	DI water	25 °C	[69]
$Ti_3C_2T_X$-coated fabric	Fe/Fe	EDL + photothermal effect	72	0.33	0.118	3,000 s unchanged (V_{oc})	/	3.5 wt% NaCl	Room temperature	[72]
$Ti_3C_2T_X$/GQDs aerogel	Pt/CNT	EDL + photothermal effect	0.25	0.8	184	12,000 s unchanged (V_{oc} and I_{sc})	45.6	3.5 wt% NaCl	Room temperature	[74]
NaV_3O_8/$Ti_3C_2T_X$ film	Au/Au	EDL + Photothermal effect	4	0.8	14.5	250 s unchanged (V_{oc} and I_{sc})	2.6	0.1 M NaCl	Room temperature	[73]
MXene/GO@PVDF/SA film	Ag/Ag	EDL + Photothermal effect	0.28	0.218	0.85 nA	400 s unchanged (V_{oc} and I_{sc})	/	3.5 wt% NaCl	25 °C	[70]
Biological fibrils/$Ti_3C_2T_x$ aerogel	Pt/Pt mesh	EDL + photothermal effect	0.785	0.35	7.64	200 min unchanged (V_{oc})	/	10^{-3} M NaCl	25 °C	[71]

volumes of liquid water, significantly expanding their potential applications, particularly in flexible and wearable sensor devices. Furthermore, MXene exhibits excellent photothermal effects, enabling enhanced water evaporation efficiency under light irradiation, which further improves power generation performance.

Several planar MXene-based EEGs utilizing water droplets as the water source have been developed, demonstrating unique power generation performance and promising application potential. These droplets first wick into one side of the active layer and gradually diffuse to the other side via capillary action and water evaporation. During this process, streaming potential is generated as water molecules flow along the surface of MXene nanosheets. Bae *et al.* reported a high-performance $Ti_3C_2T_x$-based EEG, where $Ti_3C_2T_x$ nanosheets coated on cotton serve as the electricity-generating layer [Figure 6C][67]. As shown in Figure 6D, the EEG achieved a maximum V_{oc} of 0.24 V and I_{sc} of 120 μA as a 30 μL water droplet wicked and diffused through MC. The current profile exhibited two peaks: a large initial peak during rapid wicking due to hydrophilicity and capillary channels of $Ti_3C_2T_x$, and a smaller peak at the drying stage, attributed to reduced resistance from water molecule removal [Figure 6E and F]. Further studies revealed that salt solutions of different metals can enhance voltage and

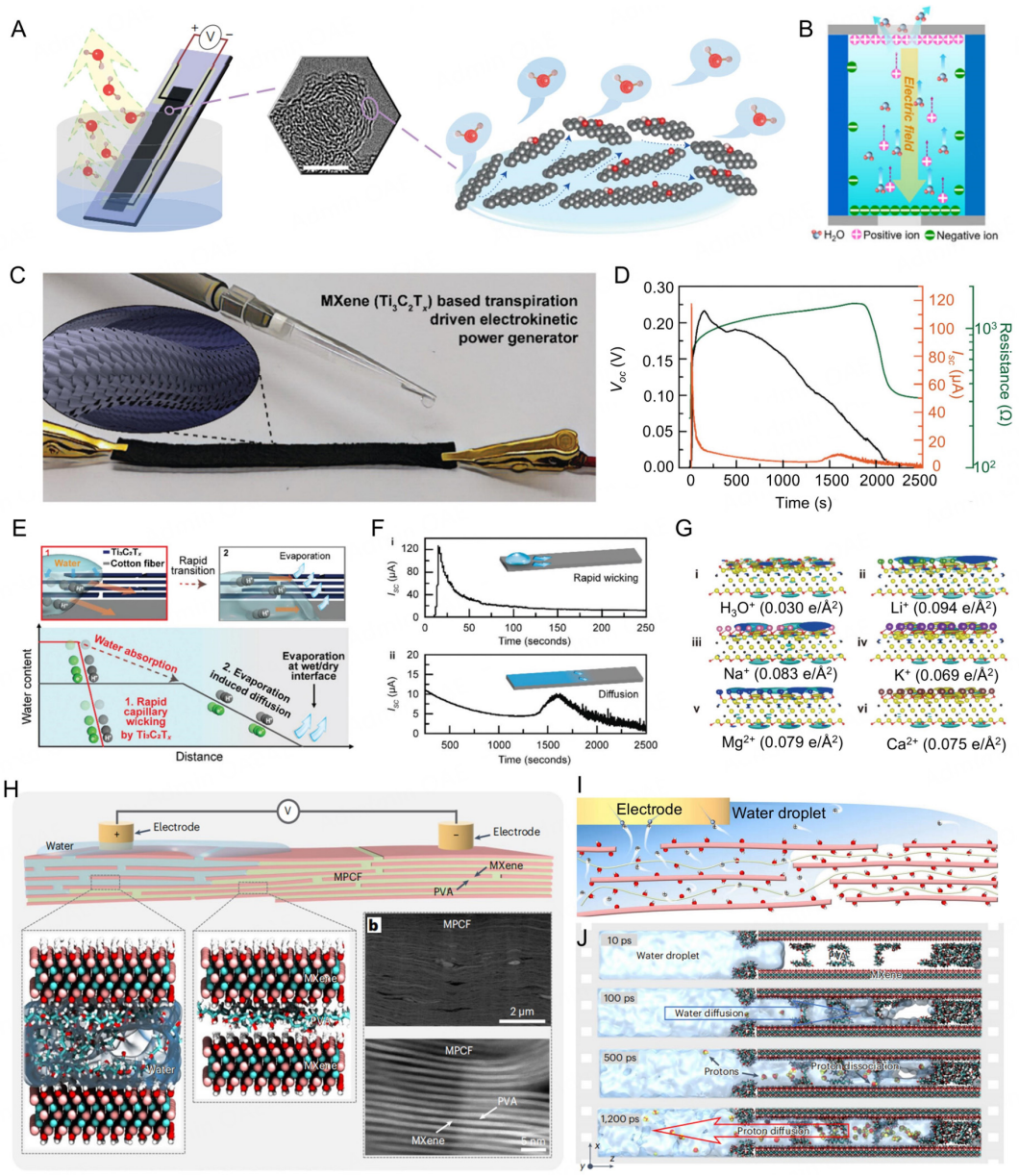

Figure 6. Working mechanism of EEGs and representative MXene-based EEGs. (A) Schematic illustration of typical experimental setup for EEGs and water flow between carbon black nanosheets induced by evaporation. Reproduced with the permission of Ref.[65] Copyright © 2017 Springer Nature. (B) Working mechanism of EEG device. Reproduced with the permission of Ref.[44] Copyright © 2023 Elsevier Ltd. (C) Photograph showing the operation of MXene-based EEG induced by droplets. (D) V_{oc}, I_{sc}, and resistance curves of MXene-based EEG with one water drop wicking. (E) Schematic illustration of working mechanism including rapid wicking and slow diffusion. (F) Two typical I_{sc} peaks initiated by wicking and diffusion. (G) Surface charge density of water molecules and different ions on the surface of MXene sheets calculated by DFT. Reproduced with the permission of Ref.[67] Copyright © 2022 Royal Society of Chemistry. (H) Schematic illustration of device structure of MPCF and corresponding channel's structure. (I) Schematic of the upstream proton diffusion mechanism. (J) MD simulations for protons dissociation and diffusion in the MXene channel. Reproduced with the permission of Ref.[69] Copyright © 2024 Springer Nature.

current output by increasing surface charge density, which is validated by DFT calculations [Figure 6G]. Similarly, Su *et al.* reported a high-performance, sweat-powered wearable EEG using single-layer MXene-coated wool cloth[68]. Active Zn electrodes enhanced output via potential chemical reactions. Electrolytes in sweat (NaCl, $CaCl_2$, KCl) infiltrate the MXene surface, increasing surface charge density and lowering the

EDL dielectric constant compared to pure water. Consequently, the MXene-based EEG achieved very high performance with a peak V_{oc} of 0.687 V, I_{sc} of 1,994 μA, and a power density of 683 μW cm^{-2}.

Unlike the streaming potential-based power generation mechanism observed in all previous EEG devices, which relies on downstream ion diffusion, a novel upstream proton diffusion mechanism has been discovered in MXene-based EEG devices. This device utilizes an MXene/PVA composite film (MPCF) as the power-generating material, with two inert Pt electrodes positioned at opposite ends of the MPCF[69]. When 5 μL of water is applied to one electrode, it exhibits a higher potential of 400 mV for over 330 min, opposite to conventional EEG behavior [Figure 6H]. Unlike fast wicking of MC, MPCF shows slower water permeation due to dense PVA molecules impeding diffusion through nanopores. Water entering MXene channels releases protons, creating a proton gradient that drives protons back into bulk water [Figure 6I]. When connected, electrons flow from the dry to the wet Pt electrode, completing the circuit. MD simulations confirmed this proton diffusion mechanism [Figure 6J], revealing a novel upstream proton transport in MXene/PVA films and offering new insights into EEGs.

To further enhance the power generation performance of EEGs, the photothermal effect of MXene was integrated into the device, thereby enhancing water evaporation rates and improving power generation efficiency[70,71]. More interestingly, when seawater is used as the working fluid, this device not only generates electricity but also enables seawater desalination. Inspired by tree water transport and leaf evaporation, Peng *et al.* designed a photothermal EEG with asymmetrically deposited $Ti_3C_2T_x$ on cotton, achieving both power generation and salt-resistant solar desalination [Figure 7A][72]. In this device, capillary action draws water into the MXene/cotton composite, generating an EDL effect that directs H^+ and Na^+ through nanochannels, producing a V_{oc} of 0.363 V. Simultaneously, photothermal effect of Mxene enhances water evaporation, enabling seawater desalination with an efficiency of 1.38 kg m^{-2} h^{-1} under sunlight. Similarly, Park *et al.* reported a bilayer MXene/sodium vanadium oxide (SVO) EEG. In this design, negatively charged SVO nanorods (a p-type semiconductor) were deposited on the substrate as the first layer, followed by a layer of MXene nanosheets[73]. The MXene layer generates the photothermal effect by absorbing sunlight. As shown in Figure 7B, immersion in water or electrolyte drives capillary flow into SVO nanochannels, generating an EDL effect and selective ion transport. MXene's photothermal effect boosts ion diffusion and conductivity via a higher temperature gradient than a single SVO layer. Using 0.1 M saltwater, this EEG can achieve a high V_{oc} of 0.8 V and I_{sc} of 30 μA at room temperature.

The biomimetic multilayer design of EEGs, combined with the integration of photothermal effects, holds great potential for further enhancing the power generation performance of the device. Inspired by lotus leaves, Chen *et al.* developed an interfacial evaporation-driven hydrovoltaic generator (IEHVG) with a multilayered biomimetic structure [Figure 7C][74]. The device consists of three layers: a bottom aerogel with vertically aligned channels for rapid water diffusion, a middle MXene/graphene quantum dots (GQD)-coated aerogel for electricity generation, and a top octadecyltrichlorosilane (OTS)-coated gradient hydrophobic layer to enhance evaporation [Figure 7D]. The MXene/GQDs layer provides high electronegativity, photothermal properties, and conductivity, ensuring strong power generation. The OTS layer creates a thermal and ionic concentration gradient, confirmed by numerical simulations and experiments [Figure 7E]. The high energy-harvesting efficiency of the IEHVG stems from rapid evaporation, the EDL effect, and gradient thermal diffusion, with the contribution of each factor summarized in Figure 7F.

MXene-based EEG devices have been extensively studied across various aspects, including material composition, power-generating water sources, multilayer structural designs, novel power generation

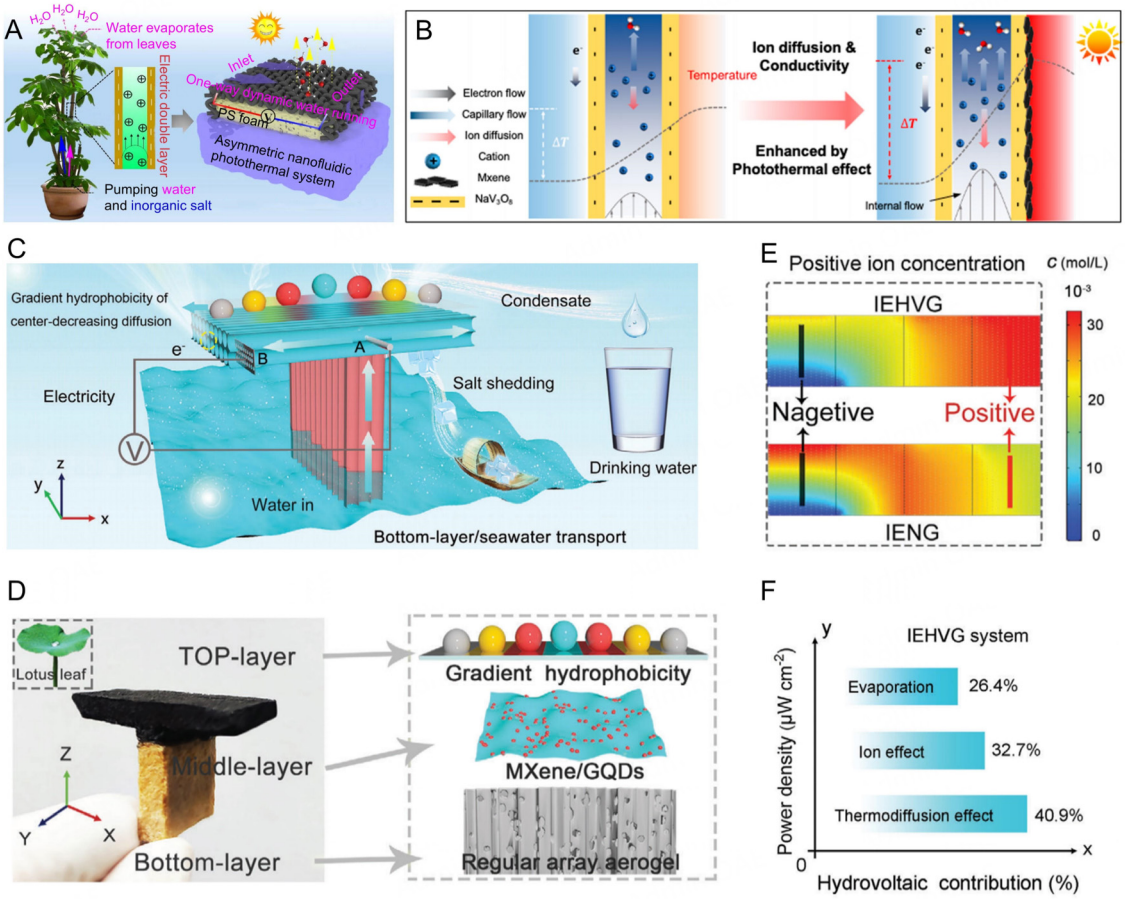

Figure 7. Photothermal effect-enhanced EEG devices. (A) Schematic illustration of pump-inspired MXene-based EEG. Reproduced with the permission of Ref.[72] Copyright © 2021 American Chemical Society. (B) Schematic illustration of photothermal effect-enhanced MXene/SVO EEG. Reproduced with the permission of Ref.[73] Copyright © 2024 American Chemical Society. (C) Schematic diagram of the working process of IEHVG. (D) Device structure of IEHVG. (E) The comparison of positive ion concentration for IEHVG and IENG. (F) Schematic representation of the hydrovoltaic contribution in the IEHVG system. Reproduced with the permission of Ref.[74] Copyright © 2024 Wiley-VCH.

mechanisms, and photothermal coupling, yielding significant research progress. However, it is important to note that most EEG devices still rely on large volumes of liquid water as the primary power-generating source, which poses a major limitation for practical applications.

MXene-based REGs

Working mechanism of REGs

The osmotic pressure difference between river water and seawater is a promising renewable energy source, known as osmotic energy, first proposed for power generation by Loeb in 1975. The RED method is one of the most promising approaches for harnessing osmotic energy[75]. Devices that operate on the RED principle are referred to as REGs.

An REG system consists of selectively permeable membranes placed between two salt solutions with different concentrations, connected to an external circuit via non-polarizable Ag/AgCl electrodes. Within this salinity gradient, ions from the high-concentration solution migrate naturally toward the low-concentration solution. When ions selectively diffuse through the membranes, osmotic potential energy is released, captured, and converted into electrical energy. However, if the channel lacks ion selectivity for

cations and anions, the net ion flux will be zero, as the flows of cations and anions cancel each other, resulting in no current generation. This highlights two critical requirements for REG electricity generation: (1) A salinity gradient between the solutions; and (2) Differential diffusion rates for cations and anions. The channels of selectively permeable membranes are the primary determinants of REG performance.

Enhancing power output requires improving both ion selectivity and permeability, which depends on designing channels with optimal structural and chemical properties. In charged nanochannels, the EDL effect promotes preferential transport of counterions while repelling co-ions. When the channel radius approaches or is smaller than the Debye length, EDL overlap occurs, excluding co-ions and allowing only counterions to diffuse through the channel. This dramatically increases ion selectivity. However, reducing the channel radius to enhance selectivity often decreases ion permeability, creating a trade-off between the two parameters. Addressing this trade-off - achieving high selective transport while ensuring efficient ion passage - is critical for optimizing osmotic energy harvesting. To maximize power density, channel density, size, and charge characteristics must be carefully optimized. By striking a balance between ion selectivity and permeability, high-performance REG systems can be designed to harness salinity gradient energy effectively.

Since MXene was introduced into REGs in 2018, it has garnered extensive research attention. To enhance the performance of MXene-based REGs, significant efforts have been made across multiple dimensions. This section provides a comprehensive review of modification strategies, focusing on the following three aspects: (1) Surface modification and structural assembly of pure MXene materials; (2) Development of various MXene-based composite materials; and (3) Incorporation of additional effects, such as photothermal effects, to boost REG performance.

Advances in pure MXene-based REGs

MXene lamellar membranes with different compositions can be directly utilized in REGs. Hong *et al.* prepared $Ti_3C_2T_x$ MXene lamellar membranes via vacuum filtration and systematically studied the influence of various parameters on REG performance, including salinity gradient, pH, membrane thickness, and temperature[76]. From the measured conductance in a 10 mM KCl solution at pH 6.3, they observed a surface charge density as high as ≈100 $mC{\cdot}m^{-2}$, surpassing those of GO laminates (50-60 $mC{\cdot}m^{-2}$), perforated graphene (~40 $mC{\cdot}m^{-2}$), and MoS_2 nanopores (20-80 $mC{\cdot}m^{-2}$ at pH 5). This high surface charge density plays a critical role in enabling highly cation-selective ion flow through the MXene nanochannels. Additionally, as the pH increases, the dissociation of terminal groups results in more negative surface charges and higher surface charge density on individual MXene nanosheets. When evaluating the MEG performance of membranes with varying thicknesses, it was found that power density strongly decreases with increasing membrane thickness. This decline is likely due to the longer channel length in thicker membranes, which hinders ion flux beyond a certain thickness. Under an optimized salinity gradient of 1000-fold, the membrane achieved a record-high output power density of 21 $W{\cdot}m^{-2}$ at room temperature and an energy conversion efficiency (η) of up to 40.6%.

MXenes with other composition such as $Mo_2TiC_2T_x$ have also been studied for their application in REGs. Chang *et al.* fabricated lamellar membranes using $Mo_2TiC_2T_x$ MXene through a similar method and further enhanced their REG performance via alkali immersion treatment[77]. After soaking the membrane in an alkaline solution with pH = 9, the V_{oc} increased significantly to 83 mV, compared to 48 mV at pH = 5. A similar trend was observed for the I_{sc}. Additionally, the membrane's cation transference number (t^+), defined as the ratio of current carried by cations to the total current and indicative of ion selectivity, improved from 0.90 under neutral conditions to 0.95 after alkaline treatment. This indicates that the treated membrane

achieved a remarkably high level of cation selectivity. The study revealed that the pH-dependent REG performance is closely linked to the deprotonation and protonation processes on the MXene surface, which significantly affect surface charge density and ion transport properties. Moreover, the membrane demonstrated excellent long-term stability, maintaining its performance over 120 h of continuous testing, showcasing its potential for durable and efficient energy harvesting applications.

MXene lamellar membranes have also been utilized to harvest energy from proton gradients, laying the groundwork for using acidic industrial wastewater with varying proton concentrations in REGs. To generate electricity from acidic solutions, it is essential to ensure that REG devices can maintain long-term stability in acidic environments. MXene offers inherent advantages in this regard, as its nanosheets are produced via acid-assisted etching processes, granting them exceptional acid resistance. Qin *et al.* investigated the REG performance of $Ti_3C_2T_x$ MXene lamellar membranes in various acidic solutions, including HCl, KCl, H_2SO_4, and H_3PO_4, and found that the output voltage and current followed the trend HCl > KCl > H_2SO_4 > H_3PO_4[78]. This trend indicates that under the same proton gradient, anions in the interlayer channels impede cation transport, with the blocking effect intensifying as the anion radius increases (Cl^- < SO_4^{2-} < PO_4^{3-}), leading to reduced output voltage and current. MD simulations further revealed that under the same anion type and concentration, hydrogen ions with smaller hydrated ion diameters move significantly faster than potassium ions. Consequently, HCl solutions exhibit superior REG performance among the tested acids. Under optimized conditions with a 1,000-fold concentration gradient in HCl, the membrane achieved a high power density of 6.5 W m^{-2}, outperforming the commercial benchmark (5 W m^{-2}) by 30%, and demonstrated stability for over 200 h at pH = 0.

Tuning the ion transport pathways within MXene membranes is an effective strategy to enhance REG performance. Dong *et al.* demonstrated the fabrication of an ultrathin MXene membrane with horizontal transport (H-MXM) through ultrathin sectioning[79]. This unique membrane design incorporates straight and ultrashort subnanochannels, functioning as an "ion freeway" that enables ultrafast ion transport. When employed for osmotic energy conversion, H-MXM achieved an impressive power density of 93.6 W·m^{-2} under a 50-fold NaCl concentration gradient, outperforming most macroscopic 2D membranes. Further studies on KCl ion transport revealed that the diffusion current density in the horizontal transport mode is nearly 40 times higher than that in the vertical transport mode, highlighting the exceptional ion transport efficiency of the horizontal "ion freeway". In another approach, Hong *et al.* developed porous MXene membranes by intentionally introducing nanosized holes into MXene sheets using a facile, scalable H_2SO_4-based etching method[80]. The resulting membranes featured shortened and continuous charge-transport pathways, enabling faster ion transport across the lamellar structure. This design simultaneously enhanced permeability and ion selectivity, overcoming the inherent trade-off between the two properties. The nanoporous $Ti_3C_2T_x$ MXene membranes achieved a maximum power density of 17.5 W·m^{-2} under a 100-fold KCl concentration gradient at neutral pH and room temperature, representing a 38% increase compared to pristine membranes. Surface modification for better selectivity of cations is another common strategy to enhance the REG performance of MXene membranes. Given that coexisting anions have equal value as cations in osmotic energy conversion, the development of anion-selective membranes is both significant and promising. Wang *et al.* introduced an amination strategy using 3-aminopropyltriethoxysilane (APTES) to fabricate positively charged MXene (PCM) nanosheets, thereby imparting anion selectivity to the resulting MXene membranes[81]. The power density of these modified membranes reached a maximum of 10.98 W·m^{-2} under a natural salinity gradient, surpassing the commercial benchmark of 5 W·m^{-2}. When operating under optimized environmental conditions, the power density further increased to 20.66 W·m^{-2} through Cl^- transmembrane transport. The modified membranes also exhibited excellent stability, with an output power density attenuation of only 3% over 10 h of continuous operation.

Combining or assembling MXene materials with differently charged surfaces has also been explored to enhance REG performance. Ding *et al.* prepared self-supporting flexible membranes by vacuum filtering pristine MXene nanosheets with negatively charged surfaces (N-MXene) and surface-modified MXene nanosheets with positively charged surfaces (P-MXene), termed N-MXM and P-MXM, respectively[82]. These membranes were then assembled into an energy harvesting system comprising a three-chamber electrochemical cell. When the middle chamber was filled with 0.01 M NaCl and the side chambers with 0.5 M NaCl, cations and anions were selectively transported by N-MXM and P-MXM, respectively. This complementary ion diffusion generated a superposed electrochemical potential and ionic flux, improving energy conversion efficiency. The system achieved a V_{oc} of 176 mV and a I_{sc} of 30.2 μA under a 50-fold salinity difference. At an external resistance of 5 kΩ, the system delivered a maximum power density of 4.6 $W \cdot m^{-2}$. Hashemifar *et al.* employed a similar strategy, using wet spinning to fabricate fibers from oppositely charged MXene nanosheets[83]. Thanks to the narrow (< 2 nm) 2D nanochannels and high surface charge densities (~3.8 $mC \cdot m^{-2}$), these fiber membranes demonstrated excellent ion selectivity and transmissibility, achieving a stable power density of 12.3 $W \cdot m^{-2}$ for several months. Ding *et al.* further advanced this concept by sequentially filtering NCM and PCM onto mixed cellulose acetate substrates to create a heterogeneous MXene membrane[84]. This asymmetric membrane design exhibited ionic diode behavior with rectified current functionality, effectively preventing concentration polarization in RED and reducing Gibbs free energy losses during Joule heating. Under a salinity gradient between synthetic seawater and river water, this ionic diode membrane-based generator achieved a power density of 8.6 $W \cdot m^{-2}$, which increased to 17.8 $W \cdot m^{-2}$ at a 500-fold salinity gradient, outperforming state-of-the-art membranes.

Advances in MXene composite-based REGs

In addition to using pure MXene, the introduction of additional components to form composite materials has been widely studied to synergistically enhance REG performance. To date, a variety of materials, including inorganic materials, organic materials, and organic-inorganic hybrid materials such as metal-organic frameworks (MOFs), have been combined with MXene to create composites for REGs[85-100].

Inorganic materials, such as 2D membranes similar to MXene, including GO, boron nitride (BN), and Co-Al layered double hydroxides (LDH), have become popular choices for synthesizing composite materials for REGs[101-106]. Gao *et al.* combined 2D GO membranes with layered MXene membranes using vacuum filtration to create a 2D-2D composite membrane, which exhibits high mechanical strength, a high surface charge density, and well-defined transport channels, making it an ideal candidate for energy conversion[106]. The study revealed that incorporating GO nanosheets into MXene membranes facilitates the formation of hydrogen bonds, enhancing the binding force and significantly improving the mechanical strength of the membrane. As the GO content increased, the zeta potential of the composite membrane slightly decreased. However, the high negative zeta potential still provided excellent selective permeability for cations such as Na^+. Inspired by the efficient vertical transport of water and minerals in tree trunks, Wang *et al.* developed a bioinspired vertically aligned MXene/GO membrane, where partial reduction of GO was used to intensify the alignment[103]. In simulated seawater and artificial river water, this vertically aligned MXene/GO membrane achieved a remarkable power density of 372 $W \cdot m^{-2}$, nearly an order of magnitude higher than that of horizontally assembled membranes under similar conditions. Numerical calculations and theoretical analyses revealed that the ultrafast ion transport in the vertically aligned MXene/GO membrane is attributed to the short transport pathways, which minimize resistance during ion migration.

Yang *et al.* constructed a $Ti_3C_2T_x$ MXene-BN composite membrane for REGs, leveraging the small size and high surface charge density of BN nanosheets[105]. Incorporating BN into the pristine MXene membrane significantly reduced its internal resistance. A composite membrane containing 44 wt% BN nanosheets

achieved an output power density of 2.3 $W \cdot m^{-2}$, nearly double that of the pristine MXene membrane. In another approach, Yang *et al.* sequentially vacuum-filtered negatively charged $Ti_3C_2T_x$ MXene and CoAl-LDH nanosheets to fabricate a 2D Janus MXene/CoAl-LDH membrane[102]. This membrane demonstrated efficient asymmetric ion transport and osmotic energy harvesting without requiring additional modification. The MXene/LDH ratio played a critical role in determining the ion rectification factor, osmotic voltage, ion selectivity, and energy conversion efficiency. The Janus membrane containing 86 wt% LDH exhibited the highest rectification factor of ~6.2 in 0.1 mM NaCl solution. Under conditions of 1 M HCl/1 M NaOH, the power density increased to ~8.75 $W \cdot m^{-2}$, representing a ~17.7% improvement compared to pristine MXene.

MOF materials, with their tunable structures and exceptional regularity, hold significant potential for REGs[107-110]. Their precisely angstrom-sized channels provide an ideal confined space, offering ultrahigh ion selectivity due to the strong overlap of the EDL and the dehydration effect of hydrated ions caused by the ultra-small pores of the MOF. However, due to the challenges in forming freestanding films and the limited surface charge density of MOFs, they are more suitable to combine with MXene to create hybrid membranes. Zhou *et al.* developed MXene/ZIF-8 hybrid membranes featuring specialized angstrom/nano-scale channels using a fast current-driven method for high-performance REG [Figure 8A and B][111]. The synergistic effect between the 3.4 Å pore size of ZIF-8 and the surface charge of MXene significantly enhanced the cation selectivity. Moreover, the incorporation of ZIF-8 crystals strengthened the interlayer interactions between MXene nanosheets and reduced the interlayer spacing, facilitating faster ion transport and higher ion permeability. As a result, the hybrid membrane achieved a high current density of 1,263.3 $A \cdot m^{-2}$ at a resistance of 1 kΩ under a 500-fold concentration gradient, demonstrating remarkable ion permeability. Consequently, the MXene/ZIF-8 hybrid membrane delivered a power density of 7.18 $W \cdot m^{-2}$ when mixing artificial seawater and river water, which increased to 48.05 $W \cdot m^{-2}$ under a 500-fold concentration gradient. Numerical simulations indicated that the small nanochannels significantly enhanced ion permeability and selectivity due to the increased overlap of EDL and the reduced ion transport pathways.

Yao *et al.* utilized an anodic electrodeposition method to construct HKUST-1@MXene composite membranes [Figure 8C][112]. The uniquely oriented porous MOFs expanded the interlayer spacing of MXene, while the inherently NCM surface facilitated a synergistic effect that significantly enhanced both ion selectivity and flux. This synergy enabled the composite membrane to achieve a remarkable diffusion potential of 340.2 mV. These advancements translated into impressive power density outputs, reaching 25.3 $W \cdot m^{-2}$ under a concentration gradient of 10^6 in KCl and 17.2 $W \cdot m^{-2}$ under a gradient of 500 in NaCl. Inspired by the hierarchical structures in biological systems that facilitate ion transfer, Yang *et al.* developed bionic nano-hierarchical structures by integrating 1D MOF (MIL-53-COOH) onto a 2D MXene substrate [Figure 8D-F][113]. The synergistic effects of the bioinspired nano-hierarchical porous structure and surface charge interactions significantly enhanced the performance and stability of the nanoconfined membrane, as demonstrated by experimental characterizations and theoretical simulations. The optimized nano-hierarchical porous membrane exhibited exceptional performance, achieving a high cation selectivity of 0.95, an outstanding power density of 35.04 $W \cdot m^{-2}$, and excellent stability over one month, showcasing its potential for long-term and efficient REGs.

Lin *et al.* developed an electrolyte-stable 2D composite membrane by self-assembling Cu-tetrakis(4-carboxyphenyl)porphyrin (TCPP) nanosheets with MXene [Figure 8G-I][114]. The unique feature of this composite lies in the orderly framework channels of the Cu-TCPP nanosheets, which impart ultralow resistance to the membrane. This innovative composite membrane achieved a high power density of 49 $W \cdot m^{-2}$ by mixing salt-lake water with river water, demonstrating its exceptional REG performance.

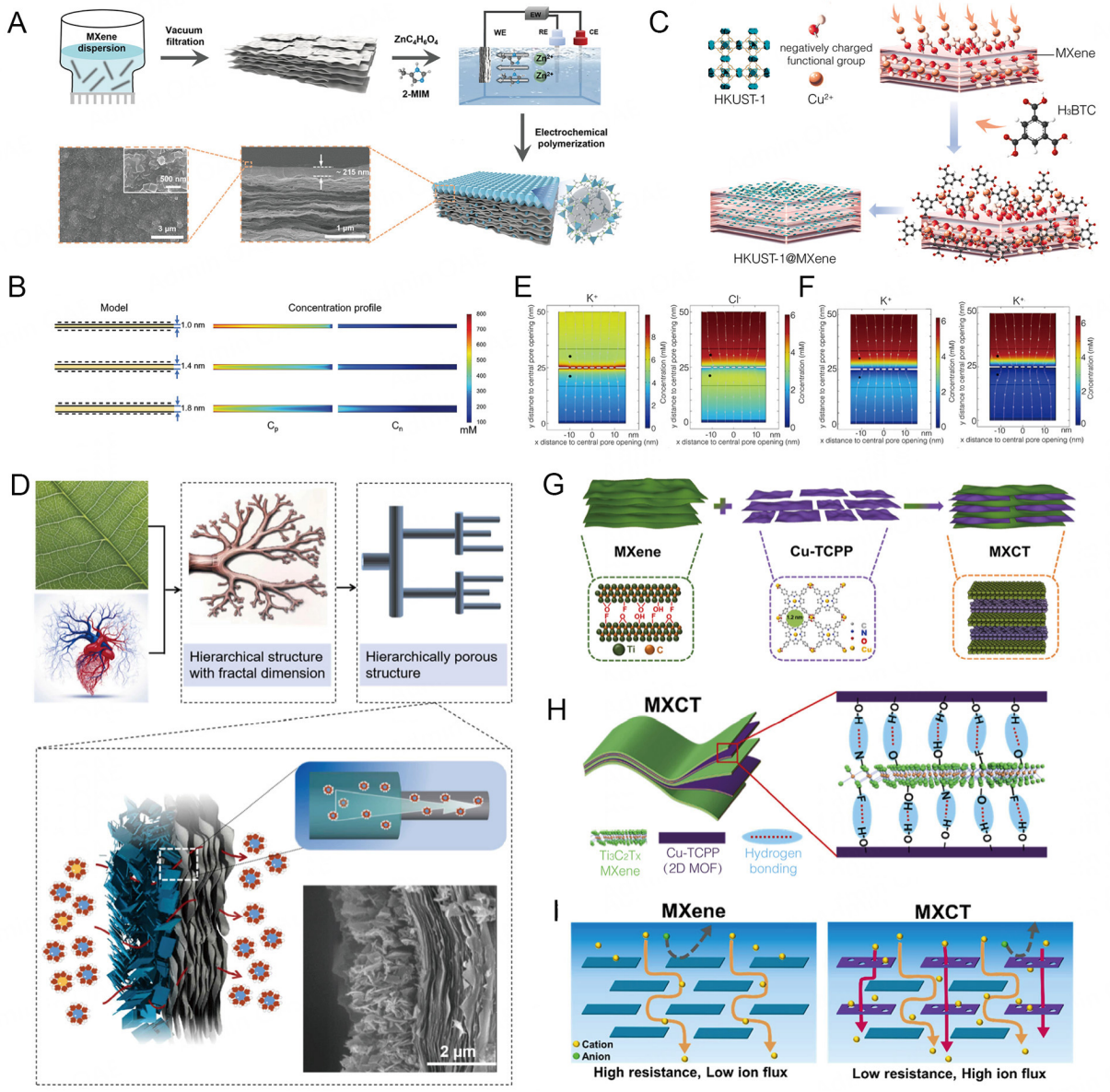

Figure 8. MOF/MXene composites for REGs. (A) Schematic of MXene/ZIF-8 hybrid membrane preparation and its microstructures. (B) Numerical simulation of ion concentration profile for cations (C_p) and anions (C_n) across 2D channels with varying distances (1.0, 1.4, and 1.8 nm). Reproduced with the permission of Ref.[111] Copyright © 2022 Wiley-VCH. (C) Schematic of oriented growth of HKUST-1 between MXene layers. Reproduced with the permission of Ref.[112] Copyright © 2024 Elsevier B.V. (D) Bioinspired design and corresponding schematic of the nano-hierarchical porous MIL-53-COOH/MXene membrane. (E) Steady-state concentration distribution of K^+ and Cl^- near MIL-53-COOH/MXene hybrid membrane. (F) Steady-state concentration distribution of K^+ near MIL-53/MXene hybrid membrane and MIL-53-NH_2/MXene hybrid membrane. Reproduced with the permission of Ref.[113] Copyright © 2024 Elsevier Ltd. (G) Schematic of MXCT membrane preparation process. (H) Schematic of interlayer structures of MXCT. (I) Schematic of the enhanced ion transport across the MXCT membrane via the incorporation of the 2D Cu-TCPP MOFs with rich sub-2 nm ion channels. Reproduced with the permission of Ref.[114] Copyright © 2024 Elsevier Ltd.

Advances in photothermal effect-enhanced MXene-based REGs

As discussed above, significant efforts have been devoted to developing REGs based on MXenes and their composites, yet their performance remains constrained. Taking advantage of excellent photothermal

properties of MXene, researchers have begun leveraging this feature to introduce additional enhancement strategies aimed at improving REG performance[115].

The photothermal effect of MXene can be utilized to regulate ion transport, enabling enhanced REG performance under concentration gradients and even reverse ion transport against concentration gradients[116]. This expands the application scenarios of MXene membranes. Liu *et al.* demonstrated that in a system with no applied voltage and equal concentrations of KCl solution (0.01 M), there was negligible ionic current initially[117]. Upon partial light irradiation of the MXene membrane (light intensity ~200 $mW \cdot cm^{-2}$), the temperature of the illuminated region rapidly increased by ~19.91 °C due to MXene's excellent photothermal properties, causing the ionic current to rise sharply to approximately 37.5 nA. When the light was turned off, both the current and temperature returned to their original states, confirming that light irradiation induces ion transport. Interestingly, the recorded ionic current flowed from the non-illuminated (low-temperature) region to the illuminated (high-temperature) region, aligning with the temperature gradient in the device. Further tests with light at wavelengths between 350-700 nm showed that at 350 nm, the temperature increase was the most pronounced, with the membrane heating from 28 to 60 °C in just 5 s. Aligning the ion current direction induced by the concentration gradient with the thermally driven ion current direction resulted in a power density of 1.68 $mW \cdot m^{-2}$, more than double the power density without illumination (0.72 $mW \cdot m^{-2}$).

Integrating light irradiation into an REG system containing wastewater can simultaneously achieve water treatment and osmotic power harvesting, as demonstrated by Xia *et al.* In this system, light irradiation not only enhanced the high permeability of Na^+ ions, increasing by 429% to 62.6 $mol \cdot m^{-2} \cdot h^{-1}$, but also demonstrated high selectivity for heavy metal ions, achieving a separation ratio of up to 2050, thus effectively treating wastewater[118]. As a result, the membrane stably generated osmotic power from simulated industrial wastewater, with the power density enhanced fourfold under light illumination at approximately one sun intensity. At a concentration gradient ratio of 500, the output power density reached an impressive 19 $W \cdot m^{-2}$.

Integrating photothermal and photoelectric effects in REG systems is expected to further enhance energy harvesting capability. Wang *et al.* developed a Janus PMMT/MXene membrane by sequentially vacuum-filtering montmorillonite (MMT) decorated with photoelectric molecules (PMMT) and MXene nanosheets[101]. The REG system constructed with this membrane enabled light-driven active ion transport, facilitating ionic energy harvesting even in electrolyte systems with equal concentrations. Under light illumination, the system generated an intramembrane electric field and a temperature gradient due to efficient charge separation and localized thermal excitation. These effects produced a PV-driven force and thermo-osmotic flow, promoting preferential ion transport. This unidirectional active transport mechanism allowed the system to achieve an output power density of 2.0 $mW \cdot m^{-2}$ and a high-performance energy conversion efficiency of 8.3×10^{-4}%.

Overall, as shown in Table 3, research on MXene-based REGs is the most extensive among all MXene-based HEGs, with a diverse range of performance enhancement strategies. These include surface modification, structural regulation, biomimetic assembly, composite formation, and photothermal coupling. These continuous advancements are driving progress in the field, offering broad application prospects and significant practical value. However, it is also important to note that current MXene materials used in REGs are predominantly $Ti_3C_2T_x$, while the MXene family comprises over a hundred different compositions. Investigating how different compositions influence interface properties, ion transport, and REG performance remains an important avenue for future research. Additionally, given the diverse range of

Table 3. Summary of reported MXene-based REGs

Functional layers	Electrodes	Thickness	Area (mm^2)	Stabilized voltage (V)	Stabilized current	Power density ($W\ m^{-2}$)	Maximum energy conversion efficiency	Long-term operation	t^+	Condition	Ref.
$Ti_3C_2T_x$ MXene lamellar membrane	Ag/AgCl	1.3 μm	1.63×10^{-2}	0.175	30 μA	21	40.6%	20 h	0.95	1 mM/1 M KCl, room temperature	[76]
$Mo_2TiC_2T_x$ MXene lamellar membrane	Ag/AgCl	4.3 μm	1.41×10^{-2}	0.083	8.9 μA	13.1	40.5%	120 h	0.95	0.5/0.01 M alkali KCl (pH = 9)	[77]
$Ti_3C_2T_x$ MXene lamellar membrane	Ag/AgCl	2.5 μm	0.03	0.3	15 μA	6.5	18.1%	200 h	0.801	1 mM /1 M HCl	[78]
ultrathin MXene membrane with horizontal transport	Ag/AgCl	3 μm	1.89×10^{-3}	-	-	93.6	-	15 days	-	0.5/0.01 M NaCl	[79]
oppositely charged $Ti_3C_2T_x$ MXene membrane assembly	Ag/AgCl	-	-	0.176	30.2 μA	4.6	-	2 months	0.96	0.5/0.01 M NaCl	[82]
$Ti_3C_2T_x$ MXene-Based Ionic Diode Membrane	Ag/AgCl	4 μm	0.03	0.089	-	8.6	39.2%	20 days	0.943	0.5/0.01 M NaCl	[84]
Porous $Ti_3C_2T_x$ MXene lamellar membrane	Ag/AgCl	0.6 μm	0.025	0.1	16 μA	17.5	46%	120 h	0.98	0.5/0.005 M KCl	[80]
oppositely charged $Ti_3C_2T_x$ MXene fiber assembly	Ag/AgCl	Diameter 30 and 20 μm	-	0.172	356 nA	12.3	45.7%	3 months	0.98	0.5/0.01 M NaCl	[83]
Aminated $Ti_3C_2T_x$ MXene membrane	Ag/AgCl	678 nm	180	-	-	10.98	-	10 h	-	0.5/0.01 M NaCl, 30 °C	[81]
$Ti_3C_2T_x$ MXene membrane+light	Ag/AgCl	~4 μm	-	-	34.39 nA	1.68 mW/m^2	-	300 s	-	0.5/0.01 M NaCl; Light intensity: ~200 $mW{\cdot}cm^{-2}$	[117]
$Ti_3C_2T_x$ MXene membrane+light	Ag/AgCl	2.2 μm	0.03	0.1	6.3 μA	5	-	400 s	-	0.5/0.01 M NaCl; Light intensity: 100 $mW{\cdot}cm^{-2}$	[118]
$Ti_3C_2T_x$ MXene/GO composite membrane	Ag/AgCl	420 nm	710	-	3.72 μA	3.7	-	10 h	-	0.5/0.01 M NaCl, 25 °C	[106]
$Ti_3C_2T_x$ MXene/GO membrane with vertical channels	Ag/AgCl	18.5-30 μm	0.26	-	-	372	-	12 h	-	0.5/0.01 M NaCl, 27 °C	[103]
$Ti_3C_2T_x$ MXene/BN composite membrane	Ag/AgCl	10 μm	0.03	0.14	78 A/m^2	2.3	~25%	10 h	0.85	0.5/0.01 M NaCl, 48 °C	[105]
Janus $Ti_3C_2T_x$ MXene/ CoAl-LDH membrane	Ag/AgCl	4.5 μm	0.03	0.13	-	8.75	-	-	-	1 M HCl/1 M NaOH, room temperature	[102]
Janus $Ti_3C_2T_x$ MXene/ montmorillonite membrane	Ag/AgCl	17.7 μm	0.2	0.0166	22.3 $\mu A/cm^2$	0.96 mW/m^2	8.3×10^{-4}%	-	-	10^{-3} M KCl, Light intensity: 25 $mW{\cdot}cm^{-2}$	[101]
$Ti_3C_2T_x$ MXene/ZIF-8 composite membrane	Ag/AgCl	2 μm	3.1	0.11	-	7.18	32.97%	16 days	0.906	0.5/0.01 M NaCl	[111]
HKUST-1@ $Ti_3C_2T_x$ MXene	Ag/AgCl	-	-	0.342	1,400 A/m^2	25.3	45.1%	-	0.92	10^6-fold KCl	[112]

composite membrane										concentration	
MIL-53-COOH/ $Ti_3C_2T_x$ MXene membrane	Ag/AgCl	4 μm	0.03	-	-	35.04	45%	30 days	0.95	0.5/0.01 M NaCl	[113]
$Ti_3C_2T_x$ MXene/Cu-TCPP membrane	Ag/AgCl	8 μm	0.03	0.09	10 μA	8.29	-	-	0.775	0.5/0.01 M NaCl	[114]

Table 4. Summary of reported MXene-based DEGs

Functional layers	Electrodes	Roles of MXene	Area (cm^{-2})	Peak V_{oc} (V)	Peak J_{sc} ($\mu A\ cm^{-2}$)	Lasting time	Droplet composition	Volume	Speed	Ref.
MXene film	Fe/Fe	EDL effect	4	0.0015	1.5	/	4 mg L^{-1} NaCl + 4 mg L^{-1} $CaCl_2$	25 μL	4 cm s^{-1}	[120]
MXene film	Ag/Ag	EDL effect	2.5	/	3.2	/	1 M NaCl	/	3 cm s^{-1}	[121]
TiO_2 (Magneli phase) film	Cu/Cu	Precursor of TiO_2	10	0.6	/	10,000 s unchanged (V_{oc})	0.1 M NaCl	100 μL	14 mL min^{-1}	[122]

modification strategies, conducting quantitative studies to systematically evaluate their effectiveness in enhancing device performance would be highly meaningful. Such an approach could provide valuable insights into the relative impact of different modification methods, facilitating the development of more optimized and efficient strategies.

MXene-based DEG

Working mechanism of DEG

The DEG utilizes a droplet sliding on the surface of an active material to generate a drawing potential. In 2014, Yin *et al.* reported for the first time DEG devices utilizing graphene film as active material[119]. When a NaCl droplet slides on the surface of graphene, it can generate a voltage of about 0.15 mV, which is named the drawing potential [Figure 9A]. The authors further provide an explanation for the generation of the drawing potential by means of a pseudocapacitive mechanism. When a droplet slides across a graphene surface, cations at the leading edge tend to adsorb onto the graphene due to the difference in contact angle between the front and rear ends of the droplet. This adsorption induces the accumulation of electrons in the graphene, facilitating pseudocapacitive charging. Conversely, at the trailing edge, cations desorb from the graphene surface, releasing the accumulated electrons and resulting in pseudocapacitive discharging. Consequently, the electron density at the trailing edge of the droplet remains higher than that at the leading edge throughout the sliding process, creating a potential gradient along the sliding direction of the droplet [Figure 9B].

MXene, another 2D material such as graphene, has also been explored for its potential in DEGs. Table 4 summarizes and compares in detail the performance of reported MXene-based DEGs.

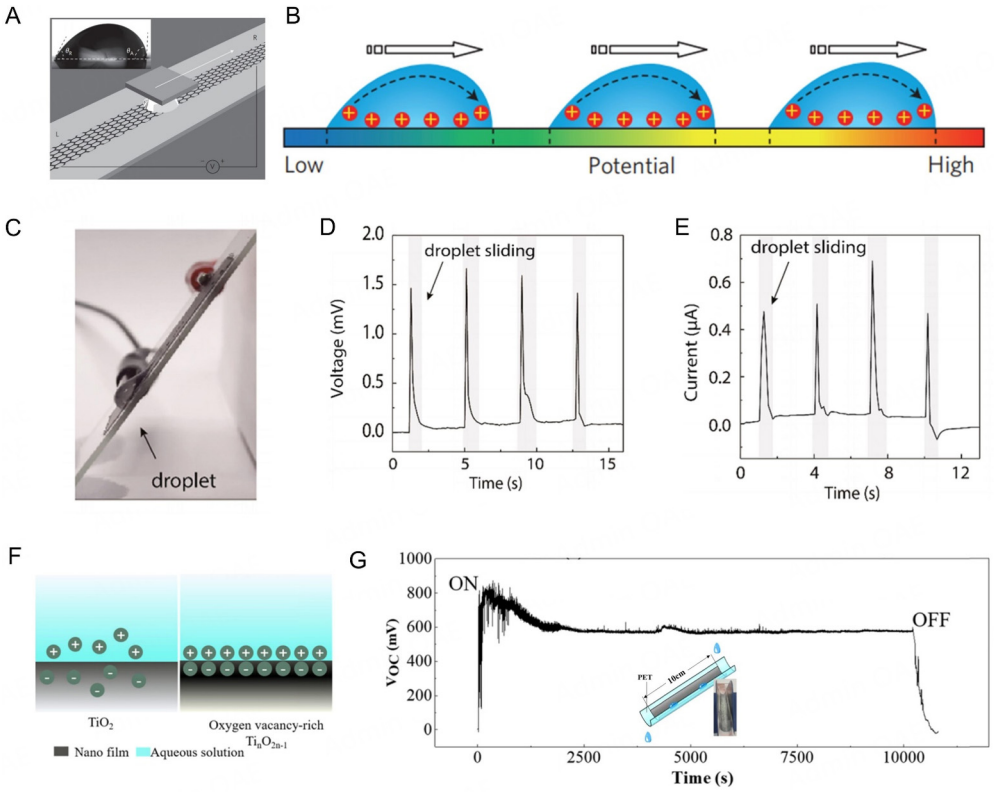

Figure 9. MXene-based DEG. (A) Schematic illustration of setup for generating electricity via sliding droplet on the graphene. (B) Schematic diagram showing the potential difference along the droplet sliding. Reproduced with the permission of Ref.[119] Copyright © 2014 Springer Nature. (C) Photograph showing the MXene film attached to the glass substrate to form the DEG device. (D) V_{oc} and (E) I_{sc} generated by droplets sliding (4 cm s^{-1}) on the MXene film with a height of 15 cm. Reproduced with the permission of Ref.[120] Copyright © 2022 American Chemical Society. (F) EDL effect formed between water and surface of TiO_2 and oxygen vacancy-rich Ti_2O_{2n-1}. (G) Long-term DEG performance test with droplet sliding speed of 14 mL min^{-1}. Reproduced with the permission of Ref.[122] Copyright © 2021 American Chemical Society.

Advances in MXene-based DEG

Bai *et al.* fabricated a 1 cm × 4 cm MXene film on a glass substrate with electrodes connected at the top and bottom ends to construct a DEG device [Figure 9C][120]. Then 25 μL droplets of an electrolyte containing 4 mg L^{-1} NaCl and 8 mg L^{-1} $CaCl_2$ were dropped from a height of 15 cm, sliding across the MXene film at a speed of approximately 4 cm s^{-1}. Under these conditions, the DEG device generated a V_{oc} of 1.5 mV and a I_{sc} ranging from 0.5 to 0.6 μA [Figure 9D and E]. The underlying mechanism was attributed to pseudocapacitance, as proposed by Lao *et al.* further investigated the performance of pure MXene films (0.5 cm × 5 cm) as DEG active materials[121]. By increasing the electrolyte concentration to 1 M NaCl, the I_{sc} was enhanced, reaching 1.6 μA at a sliding speed of 0.5 cm s^{-1}. The I_{sc} exhibited a positive correlation with sliding speed, peaking at 8 μA at a speed of 3 cm s^{-1}. These results demonstrate that the I_{sc} of pure MXene-based DEG devices can be effectively modulated by adjusting the ion concentration and sliding speed of the droplets.

However, the V_{oc} remained low due to the high electrical conductivity of the MXene film. To overcome this, Si *et al.* used $Ti_3C_2T_x$-derived materials to fabricate oxygen vacancy-rich $TinO_{2n-1}$ films via calcination[122]. Peroxo-titanic acid gels were synthesized by mixing $Ti_3C_2T_x$ with H_2O_2, then calcined in hydrogen at 800 °C to form TiO_2 films. At 1,000 °C, TiO_2 transformed into Ti_4O_7 due to oxygen removal. Oxygen vacancies on the Ti_4O_7 surface enabled denser EDL formation, enhancing cation adsorption and DEG performance

[Figure 9F]. Raising the calcination temperature from 800 to 1,000 °C increased V_{oc} from 17 to 83 mV and I_{sc} from 0.015 to 0.52 μA. To further improve performance, the authors designed a 10 cm tubular DEG coated with TiO_2 films. Using 0.1 M NaCl and droplets sliding at 14 mL min^{-1}, the device achieved a stable 0.6 V V_{oc} over 10,000 s [Figure 9G], highlighting the potential of MXene-based DEG as a reliable power source.

COUPLING OF MXENE-BASED HEGS WITH OTHER ENERGY-HARVESTING SYSTEMS

In the preceding sections, we reviewed various strategies for enhancing MXene-based HEGs, primarily focusing on improvements to HEG materials and device design. However, due to the inherent limitations in energy input and conversion efficiency, their power generation performance remains far from satisfactory.

Integrating other energy harvesting systems such as TENGs, TEGs, and PVs, with HEGs holds great promise for introducing additional energy inputs, thereby significantly boosting power generation performance[123-127]. More importantly, such coupled designs could enable multimodal self-powered sensing applications, effectively expanding their potential use cases[128-135].

Coupling of MXene-based HEG with TENGs

Since a TENG converts external mechanical stimuli into AC output based on the coupling of triboelectrification and electrostatic induction, it exhibits high voltage (> 100 V) and low current (< 10 μA), complementing the output of MEGs. However, the challenge in integrating these generators lies in their differing humidity dependencies. MEGs typically generate lower output at low humidity but significantly improve under high humidity. In contrast, excessive moisture easily neutralizes triboelectric charges in TENGs, reducing charge transfer efficiency at the friction interface, leading to optimal performance under low humidity.

To achieve complementary integration of TENGs and MEGs, Kim *et al.* reported a flexible hybrid energy generator (HEG) based on a MXene/organo-ionic hydrogel foam (MOHF) [Figure 10A][51]. Benefiting from this bilayer structural design, the hydrogel provides sufficient water to the MXene active layer, allowing the MEG to function independently of external humidity. Even at 20% RH, the device achieves a V_{oc} of 0.3 V and an I_{sc} of 100 μA. The top surface of the MOHF, unwetted by the bottom hydrogel, serves as the friction layer for the TENG. When a Perfluoroalkoxy (PFA) film undergoes contact-separation with MOHF, the electronegativity difference between PFA and MOHF induces electron transfer at the interface, generating a corresponding V_{oc} or I_{sc} change in the external circuit [Figure 10B]. For MOHF, the power generation processes of TENG and MEG operate independently, with MEG relying on internal cations migration and TENG on surface electron transfer [Figure 10C]. Therefore, to achieve hybrid output, both signals can be simultaneously collected using a parallel circuit [Figure 10D]. Comparison tests showed that when TENG and MEG operate simultaneously, the MOHF hybrid generator achieves a V_{oc} of 55 V and an I_{sc} of 100 μA, demonstrating complementary integrated output [Figure 10E and F].

Coupling of MXene-based HEGs with thermoelectric generators

TEGs based on Seebeck effect convert thermal energy directly into electrical energy by utilizing a temperature gradient to drive charge carrier migration, generating an electric current. Meanwhile, the MEGs operate based on asymmetric water molecule adsorption, which creates an ion gradient within the active material. Ion diffusion generates an ionic current, inducing an electron current in the external circuit. Synthesizing an active material with both TEG and MEG properties is key to achieving TEG-MEG coupling. Xue *et al.* introduced a sandwiched Janus-structured thermo-hydroelectric generator (THEG) based on 1T-MoS_2/Csilk (MCs) and 1T-MoS_2/MXene-Cotton (MMC)[49]. Due to van der Waals interactions between MoS_2 and MXene nanosheets, MMC exhibits n-type conductivity, while MC shows p-type conductivity due

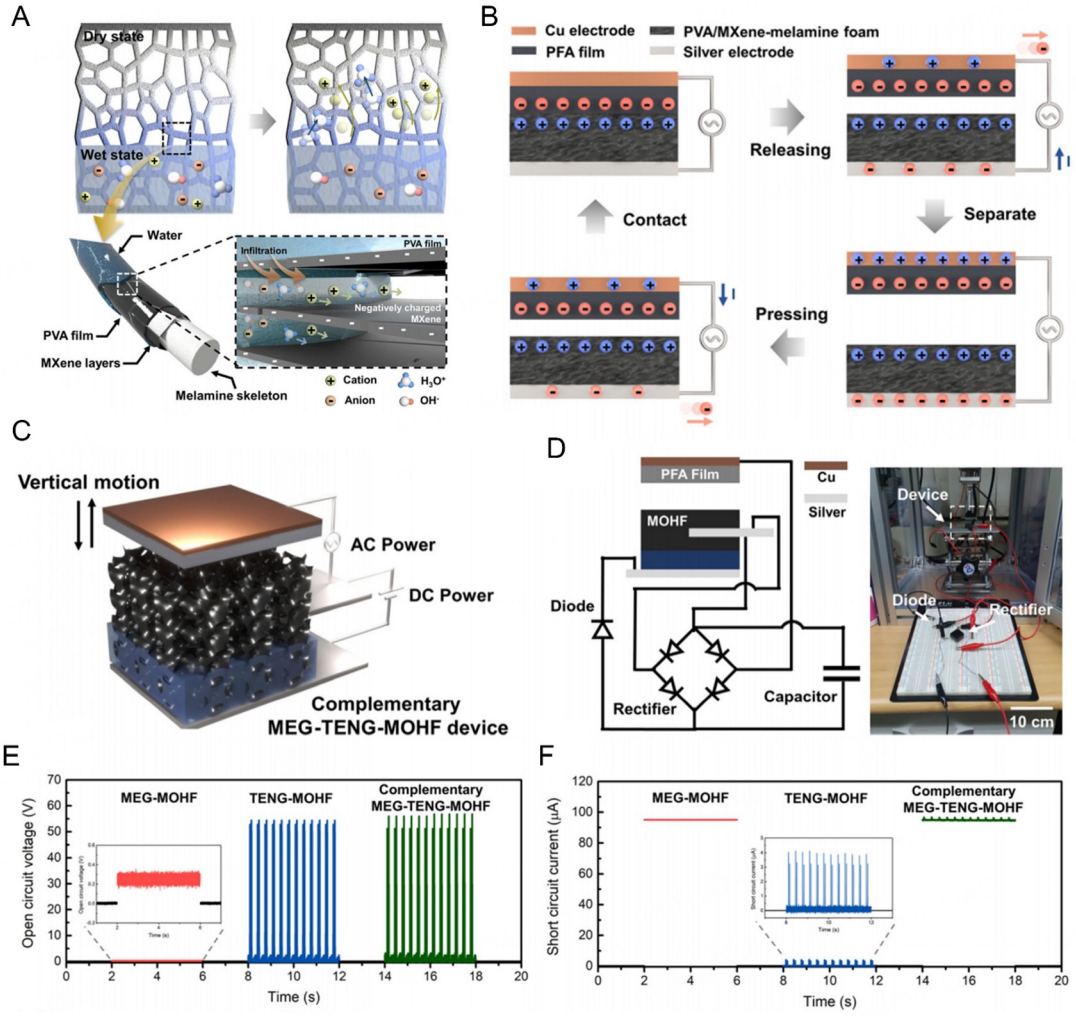

Figure 10. Coupling of MXene-based HEG and TENG. (A) Schematic showing working mechanism of MXene-based MEG. (B) Working principle of contact separation type TENG consisting of PVA/MXene-melamine foam and PFA film. (C) Schematic diagram explaining the structure of complementary MEG-TENG-MOHF device. (D) Schematic diagram and photograph of the external circuit integrating the TENG and MEG outputs. (E) V_{OC} and (F) I_{SC} for the MEG-MOHF, TENG-MOHF, and complementary MEG-TENG-MOHF. Reproduced with the permission of Ref.[51] Copyright © 2024 Royal Society of Chemistry.

to the presence of MoS_2. As a result, the MMC/MC structure enables TEG performance detection under a temperature gradient [Figure 11A]. Within a temperature difference range of 0-20 K, the Seebeck coefficient is 2.35 μV K^{-1} [Figure 11B]. Additionally, due to the oxygen-containing functional groups on MXene nanosheets, MMC can serve as the active layer for MEG, with MC and Al acting as MEG electrodes. Under these conditions, the THEG exhibits MEG output [Figure 11C]. Due to the Janus-type MMC/MC active layer possessing both TEG and MEG properties and sharing a common external circuit, both generate a continuous DC output. As a result, THEG enables coupled output under simultaneous temperature and moisture gradients. Under dry conditions, the device generates a V_{oc} of 0.825 mV via the TEG effect at a ΔT of 30 K. Upon sweating, the MEG effect significantly enhances the V_{oc} to 1.236 V [Figure 11D]. These findings underscore the potential of integrating TEG and MEG mechanisms in wearable electronics, providing a versatile and efficient solution for self-powered systems.

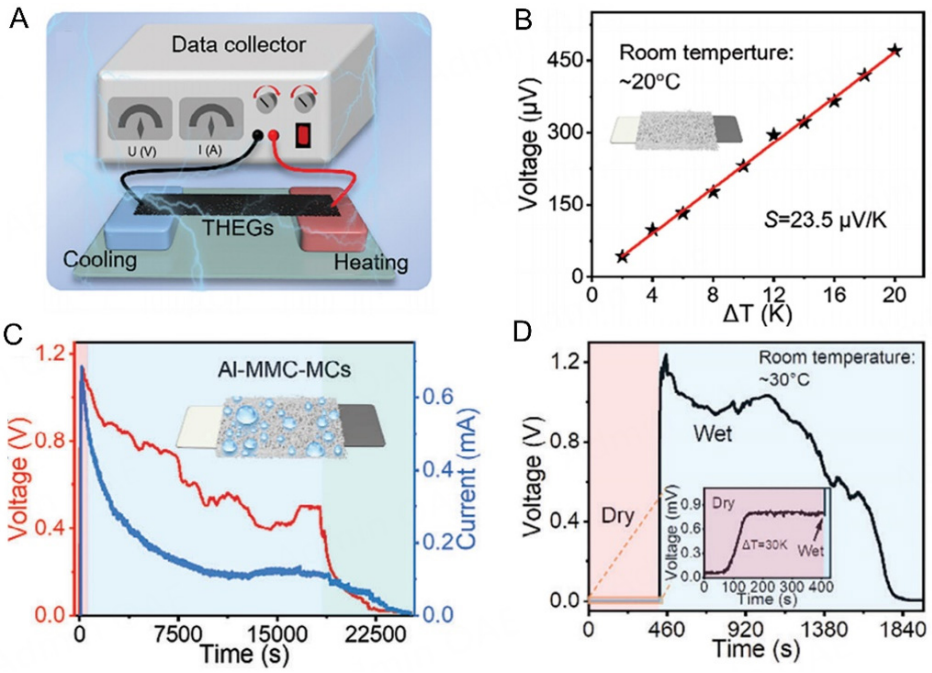

Figure 11. Coupling of MXene-based HEG and TEG. (A) Schematic of thermoelectric measurement for MCs-MMCs THEGs. (B) Corresponding Seebeck coefficient with the ΔT range of 0-20 K. (C) V_{oc} and I_{sc} output of HEG based on the structure of Al-MMC-MCs (D) V_{oc} curves demonstrating the wearable THEG exhibits TEG and HEG power generation in dry and wet states, respectively. Reproduced with the permission of Ref.[49] Copyright © 2024 Wiley-VCH.

CONCLUSION AND PERSPECTIVES

In this review, we have provided a comprehensive summary of the development of MXene in the field of HEGs, focusing on four key aspects: MEGs, EEGs, DEGs, and REGs. We have detailed various strategies for MXene, including surface modification, structural assembly, and composite formation, for boosting HEG performance.

Overall, in terms of research volume, current HEG studies utilizing MXene have advanced more extensively and rapidly in MEGs and REGs, whereas research on DEGs remains in its early stages. Regarding device configurations, most MXene-based HEGs are fabricated in the form of 2D thin films, while devices with other dimensional structures are still rare, potentially limiting their application scope. In terms of applications, the primary focus has been on power generation and sensing, yet the number of related studies remains relatively limited. Regarding the role of MXene, it has demonstrated versatility, serving multiple functions across different HEG devices: it can serve as an active material for power generation, as a conductive additive, and as a precursor material for HEG components. Among these, its role as an active material is the core focus of current research, accounting for the majority of studies, while its other applications remain in early stages of exploration. Besides, the coupling of MXene-based HEGs with other types of energy harvesting devices has only recently attracted attention, with only a few scattered studies reported to date.

As an emerging field, MXene-based HEGs are still in the early stages of development. Consequently, the performance of MXene-based HEGs is currently limited, with relatively simple structures and functionalities that require further enhancement. Looking ahead, future research should prioritize the following areas:

(1) Exploring the HEG properties of different MXene family members. Currently, $Ti_3C_2T_x$ is the primary material studied for HEGs, and its structure-property relationships have been partially understood. However, the MXene family potentially includes hundreds of members, each with unique compositions that could significantly alter their physicochemical properties. These changes may impact interactions with water molecules and the overall HEG performance. Future research should systematically explore how different MXene compositions influence HEG performance to uncover potential material candidates with enhanced capabilities.

(2) Clarifying the mechanisms and principles of MXene-based HEGs. Although the power generation mechanisms of various HEGs have been extensively studied, the understanding of MXene-based HEGs remains superficial. Theoretical models often fail to fully align with experimental observations, leading to multiple hypotheses about power generation mechanisms. To improve HEG performance and facilitate practical applications, it is crucial to develop a clear understanding of the fundamental mechanisms and principles underlying MXene-based HEG operation through combined experimental and theoretical studies.

(3) Identifying the intrinsic performance of MXene-based HEGs. In many studies, various electrodes, including non-inert electrodes such as Zn and Cu, have been used. However, such electrodes may inadvertently introduce battery-like reactions, artificially enhancing HEG performance, particularly in MEGs. This makes it challenging to accurately assess the intrinsic activity of MXene materials, potentially hindering the field's development. Establishing standardized testing protocols, such as using symmetric inert electrodes, is essential for accurately evaluating the intrinsic performance of MXene-based HEGs and ensuring the field's healthy and robust growth.

(4) Expanding the dimensions and forms of MXene-based HEG devices. The hydrophilicity and excellent dispersion of Mxene in water provide it with superior processability, enabling the fabrication of fibers, thin films, aerogels, hydrogels, and other structures. However, most MXene-based HEG devices are currently utilized in 2D thin-film forms. Future research should diversify the dimensions and configurations of MXene-based HEGs to better align with functional and application needs.

(5) Coupling with other energy harvesting devices. As demonstrated earlier, coupling MXene-based HEGs with other energy harvesting technologies not only improves power generation performance but also broadens application scenarios. However, research on coupled devices is still in its infancy, with only a few case studies available. This area presents significant opportunities for exploration.

DECLARATIONS

Authors' contributions

Conceptualization, methodology, visualization, formal analysis, writing - original draft: Li, S.; Zan, G.
Conceptualization, investigation, writing - original draft: Li, S.; Liu, J.
Methodology, writing - original draft: Zhao, K.
Software, visualization: Kim, H.
Investigation, visualization: Shin, E.
Visualization: Kim, G.
Conceptualization, funding acquisition, resources, supervision, writing - reviewing and editing: Zan, G

Availability of data and materials

Not applicable.

Financial support and sponsorship

This work was supported by the National Natural Science Foundation of China (No. 22205165).

Conflict of interest

All authors declared that there are no conflicts of interest.

Ethical approval and consent to participate

Not applicable.

Consent for publication

Not applicable.

REFERENCES

1. Zhang, Z.; Li, X.; Yin, J.; et al. Emerging hydrovoltaic technology. *Nat. Nanotechnol.* **2018**, *13*, 1109-19. DOI
2. Yin, J.; Zhou, J.; Fang, S.; Guo, W. Hydrovoltaic energy on the way. *Joule* **2020**, *4*, 1852-5. DOI
3. Wang, X.; Lin, F.; Wang, X.; et al. Hydrovoltaic technology: from mechanism to applications. *Chem. Soc. Rev.* **2022**, *51*, 4902-27. DOI
4. Poredoš, P.; Wang, R. Sustainable cooling with water generation. *Science* **2023**, *380*, 458-9. DOI PubMed
5. Zan, G.; Wu, Q. Biomimetic and bioinspired synthesis of nanomaterials/nanostructures. *Adv. Mater.* **2016**, *28*, 2099-147. DOI PubMed
6. Li, S.; Zhao, K.; Shin, E. A.; Kim, G.; Zan, G. Passive interfacial cooling sparks a major leap in solar-driven water and power cogeneration. *Clean. Energy. Sci. Technol.* **2024**, *2*, 140. DOI
7. Zan, G.; Li, S.; Chen, P.; Dong, K.; Wu, Q.; Wu, T. Mesoporous cubic nanocages assembled by coupled monolayers with 100% theoretical capacity and robust cycling. *ACS. Cent. Sci.* **2024**, *10*, 1283-94. DOI PubMed PMC
8. Pu, S.; Zan, G.; Zhou, H.; et al. Sustaining 500,000 folding cycles through bioinspired stress dispersion design in sodium-ion batteries. *Angew. Chem. Int. Ed.* **2025**, *64*, e202417589. DOI
9. Zan, G.; Li, S.; Zhao, K.; et al. Emerging bioinspired hydrovoltaic electricity generators. *Energy. Environ. Sci.* **2025**, *18*, 53-96. DOI
10. Jin, R.; Lou, Y.; Wang, Z. Deposition technologies of perovskite layer enabling large-area photovoltaic modules. *Energy. Mater. Dev.* **2024**, *2*, 9370030. DOI
11. Li, Y.; Zhang, D.; Qiao, W.; et al. Nanostructured heterogeneous photocatalyst materials for green synthesis of valuable chemicals. *Chem. Synth.* **2022**, *2*, 9. DOI
12. Park, S. M.; Wei, M.; Lempesis, N.; et al. Low-loss contacts on textured substrates for inverted perovskite solar cells. *Nature* **2023**, *624*, 289-94. DOI
13. Wang, Z. L.; Song, J. Piezoelectric nanogenerators based on zinc oxide nanowire arrays. *Science* **2006**, *312*, 242-6. DOI PubMed
14. Yang, Q.; Yang, S.; Qiu, P.; et al. Flexible thermoelectrics based on ductile semiconductors. *Science* **2022**, *377*, 854-8. DOI
15. Zahid, M.; Savla, N.; Pandit, S.; et al. Microbial desalination cell: desalination through conserving energy. *Desalination* **2022**, *521*, 115381. DOI
16. Zhao, K.; Li, S.; Zan, G.; et al. Moisture-driven energy generation by vertically structured polymer aerogel on water-collecting gel. *Nano. Energy.* **2024**, *126*, 109645. DOI
17. Xu, J.; Wang, P.; Bai, Z.; et al. Sustainable moisture energy. *Nat. Rev. Mater.* **2024**, *9*, 722-37. DOI
18. Wang, J.; Cao, X.; Cui, X.; et al. Recent advances of green electricity generation: potential in solar interfacial evaporation system. *Adv. Mater.* **2024**, *36*, e2311151. DOI
19. Liu, Z.; Liu, C.; Chen, Z.; et al. Recent advances in two-dimensional materials for hydrovoltaic energy technology. *Exploration* **2023**, *3*, 20220061. DOI PubMed PMC
20. Shin, E.; Kim, G.; Zhao, K.; et al. Environmentally sustainable moisture energy harvester with chemically networked cellulose nanofiber. *Energy. Environ. Sci.* **2024**, *17*, 7165-81. DOI
21. Zan, G.; Jiang, W.; Kim, H.; et al. A core-shell fiber moisture-driven electric generator enabled by synergetic complex coacervation and built-in potential. *Nat. Commun.* **2024**, *15*, 10056. DOI PubMed PMC
22. Peng, X.; Chen, L.; Liu, Y.; et al. Strain engineering of two-dimensional materials for energy storage and conversion applications.

Chem. Synth. **2023**, *3*, 47. DOI

23. Zhang, M.; Zhang, K.; Wei, W.; Yuan, H.; Chang, J.; Hao, Y. Arginine modification of hybrid cobalt/nitrogen $Ti_3C_2T_x$ MXene and its application as a sulfur host for lithium-sulfur batteries. *Microstructures* **2024**, *4*, 2024013. DOI
24. Dai, X.; Wang, Z.; Wang, X.; et al. MXene-based sodium-sulfur batteries: synthesis, applications and perspectives. *Rare. Met.* **2025**, *44*, 1522-55. DOI
25. Wang, X.; Yang, Q.; Meng, X.; Zhen, M.; Hu, Z.; Shen, B. Research status and perspectives of MXene-based materials for aqueous zinc-ion batteries. *Rare. Met.* **2024**, *43*, 1867-85. DOI
26. Naguib, M.; Kurtoglu, M.; Presser, V.; et al. Two-dimensional nanocrystals produced by exfoliation of Ti_3AlC_2. *Adv. Mater.* **2011**, *23*, 4248-53. DOI
27. Li, L.; Cheng, Q. MXene based nanocomposite films. *Exploration* **2022**, *2*, 20220049. DOI PubMed PMC
28. Anasori, B.; Gogotsi, Y. MXenes: trends, growth, and future directions. *Graphene. 2D. Mater.* **2022**, *7*, 75-9. DOI
29. Gogotsi, Y. The Future of MXenes. *Chem. Mater.* **2023**, *35*, 8767-70. DOI
30. VahidMohammadi, A.; Rosen, J.; Gogotsi, Y. The world of two-dimensional carbides and nitrides (MXenes). *Science* **2021**, *372*, eabf1581. DOI PubMed
31. Gogotsi, Y.; Anasori, B. The rise of MXenes. *ACS. Nano.* **2019**, *13*, 8491-4. DOI PubMed
32. Liu, Y.; Shi, Z.; Liang, T.; et al. The mechanism of room-temperature oxidation of a HF-etched $Ti_3C_2T_x$ MXene determined via environmental transmission electron microscopy and molecular dynamics. *InfoMat* **2024**, *6*, e12536. DOI
33. Ma, H.; Fang, H.; Li, J.; Li, Z.; Fang, X.; Wang, H. Transmittance contrast-induced photocurrent: a general strategy for self-powered photodetectors based on MXene electrodes. *InfoMat* **2024**, *6*, e12540. DOI
34. Cheng, X.; Guan, R.; Wu, Z.; Sun, Y.; Che, W.; Shang, Q. Establishing carrier transport channels based on Ti-S bonds and enhancing the photocatalytic performance of MXene quantum dots-$ZnIn_2S_4$ for ammonia synthesis. *InfoMat* **2024**, *6*, e12535. DOI
35. Chen, Y.; Dai, Y.; Bodepudi, S. C.; et al. High-sensitive and fast MXene/silicon photodetector for single-pixel X-ray imaging. *InfoMat* **2024**, *6*, e12596. DOI
36. Mathis, T. S.; Maleski, K.; Goad, A.; et al. Modified MAX phase synthesis for environmentally stable and highly conductive Ti_3C_2 MXene. *ACS. Nano.* **2021**, *15*, 6420-9. DOI
37. Jia, L.; Zhou, S.; Ahmed, A.; et al. Tuning MXene electrical conductivity towards multifunctionality. *Chem. Eng. J.* **2023**, *475*, 146361. DOI
38. Li, J.; Hao, J.; Wang, R.; et al. Ultra-stable cycling of organic carboxylate molecule hydrogen bonded with inorganic $Ti_3C_2T_x$ MXene with improved redox kinetics for sodium-ion batteries. *Battery. Energy.* **2024**, *3*, 20230033. DOI
39. Usman, K. A. S.; Zhang, J.; Marquez, K. P.; et al. Recent advances and opportunities in MXene-based liquid crystals. *InfoMat* **2024**, *6*, e12516. DOI
40. He, G.; Ning, F.; Liu, X.; et al. High-performance and long-term stability of MXene/PEDOT:PSS-decorated cotton yarn for wearable electronics applications. *Adv. Fiber. Mater.* **2024**, *6*, 367-86. DOI
41. Duan, S.; Lin, Y.; Shi, Q.; et al. Highly sensitive and mechanically stable MXene textile sensors for adaptive smart data glove embedded with near-sensor edge intelligence. *Adv. Fiber. Mater.* **2024**, *6*, 1541-53. DOI
42. Feng, W.; Zou, L.; Lan, C.; E, S.; Pu, X. Core-sheath CNT@MXene fibers toward absorption-dominated electromagnetic interference shielding fabrics. *Adv. Fiber. Mater.* **2024**, *6*, 1657-68. DOI
43. Zhao, F.; Cheng, H.; Zhang, Z.; Jiang, L.; Qu, L. Direct power generation from a graphene oxide film under moisture. *Adv. Mater.* **2015**, *27*, 4351-7. DOI
44. Lü, J.; Ren, G.; Hu, Q.; Rensing, C.; Zhou, S. Microbial biofilm-based hydrovoltaic technology. *Trends. Biotechnol.* **2023**, *41*, 1155-67. DOI
45. Zhang, H.; He, N.; Wang, B.; et al. High-performance, highly stretchable, flexible moist-electric generators via molecular engineering of hydrogels. *Adv. Mater.* **2023**, *35*, e2300398. DOI
46. Luo, P.; Cao, Y.; Han, B.; et al. Nanosheets array-induced nanofluidic channels toward efficient primary batteries-coordinated textiles. *Nano. Energy.* **2023**, *118*, 108988. DOI
47. Zhao, K.; Lee, J. W.; Yu, Z. G.; et al. Humidity-tolerant moisture-driven energy generator with MXene aerogel-organohydrogel bilayer. *ACS. Nano.* **2023**, *17*, 5472-85. DOI
48. Li, Y.; Wu, Y.; Shao, B.; et al. Asymmetric charged conductive porous films for electricity generation from water droplets via capillary infiltrating. *ACS. Appl. Mater. Interfaces.* **2021**, *13*, 17902-9. DOI
49. Xue, Y. B.; Cao, Y. M.; Luo, P.; et al. Asymmetric sandwich Janus Structure for high-performance textile-based thermos-hydroelectric generators toward human health monitoring. *Adv. Funct. Mater.* **2024**, *34*, 2310485. DOI
50. Zhao, Q.; Jiang, Y.; Duan, Z.; et al. A Nb_2CT_x/sodium alginate-based composite film with neuron-like network for self-powered humidity sensing. *Chem. Eng. J.* **2022**, *438*, 135588. DOI
51. Kim, G.; Lee, J. W.; Zhao, K.; et al. A deformable complementary moisture and tribo energy harvester. *Energy. Environ. Sci.* **2024**, *17*, 134-48. DOI
52. Liu, C.; Wan, T.; Guan, P.; et al. Unveil the triple roles of water molecule on power generation of MXene Derived TiO_2 based moisture electric generator. *Adv. Energy. Mater.* **2024**, *14*, 2400590. DOI
53. He, P.; Guo, R.; Hu, K.; et al. Tough and super-stretchable conductive double network hydrogels with multiple sensations and moisture-electric generation. *Chem. Eng. J.* **2021**, *414*, 128726. DOI

54. Yin, J.; Liu, N.; Jia, P.; et al. MXene-enhanced environmentally stable organohydrogel ionic diode toward harvesting ultralow-frequency mechanical energy and moisture energy. *SusMat* **2023**, *3*, 859-76. DOI
55. Li, P.; Su, N.; Wang, Z.; Qiu, J. A $Ti_3C_2T_x$ MXene-based energy-harvesting soft actuator with self-powered humidity sensing and real-time motion tracking capability. *ACS. Nano.* **2021**, *15*, 16811-8. DOI
56. Wei, J.; Jia, S.; Ma, C.; et al. Nacre-inspired composite film with mechanical robustness for highly efficient actuator powered by humidity gradients. *Chem. Eng. J.* **2023**, *451*, 138565. DOI
57. Cai, C.; Chen, Y.; Cheng, F.; Wei, Z.; Zhou, W.; Fu, Y. Biomimetic dual absorption-adsorption networked MXene aerogel-pump for integrated water harvesting and power generation system. *ACS. Nano.* **2024**, *18*, 4376-87. DOI
58. Tong, X.; Chen, G.; Ahommed, M. S.; et al. A carbon nanofiber/$Ti_3C_2T_x$/carboxymethyl cellulose composite-based highly sensitive, reversible, directionally controllable humidity actuator and generator *via* continuous track-inspired self-assembly. *J. Mater. Chem. A.* **2024**, *12*, 33003-14. DOI
59. Feng, Y.; Wang, R.; Ge, T. Full passive MOF water harvester in a real desert climate. *Device* **2023**, *1*, 100054. DOI
60. Jin, Y.; Ghaffour, N. Boosting atmospheric water harvesting with a solar-driven humidity-adaptable membrane device. *Device* **2024**, *2*, 100427. DOI
61. Qin, L.; Cao, H. Two ways to cool via passive sorption with atmospheric water. *Device* **2023**, *1*, 100187. DOI
62. Yang, X.; Xiang, C.; Wang, R. Harvesting clean energy from moisture. *Device* **2023**, *1*, 100016. DOI
63. Yu, J.; Deng, F.; Liu, H.; Wang, C.; Zou, H.; Wang, R. Passive and continuous moisture pump for humidity regulation via simultaneous water adsorption and desorption. *Device* **2024**, *2*, 100429. DOI
64. Wilson, C. T.; Cha, H.; Zhong, Y.; Li, A. C.; Lin, E.; El, F. B. Design considerations for next-generation sorbent-based atmospheric water-harvesting devices. *Device* **2023**, *1*, 100052. DOI
65. Xue, G.; Xu, Y.; Ding, T.; et al. Water-evaporation-induced electricity with nanostructured carbon materials. *Nat. Nanotechnol.* **2017**, *12*, 317-21. DOI
66. Zhang, X.; Zhang, X.; Fan, X.; et al. Fabrication and study of a high output power flexible fabric hydrovoltaic generator. *J. Mater. Chem. A.* **2023**, *11*, 26173-82. DOI
67. Bae, J.; Kim, M. S.; Oh, T.; et al. Towards Watt-scale hydroelectric energy harvesting by $Ti_3C_2T_x$-based transpiration-driven electrokinetic power generators. *Energy. Environ. Sci.* **2022**, *15*, 123-35. DOI
68. Su, H.; Usman, K. A. S.; Nilghaz, A.; et al. Efficient energy generation from a sweat-powered, wearable, MXene-based hydroelectric nanogenerator. *Device* **2024**, *2*, 100356. DOI
69. Xia, H.; Zhou, W.; Qu, X.; et al. Electricity generated by upstream proton diffusion in two-dimensional nanochannels. *Nat. Nanotechnol.* **2024**, *19*, 1316-22. DOI
70. Zhang, J.; Li, Z.; Meng, T.; et al. Monolithic all-weather solar-thermal interfacial membrane evaporator. *Chem. Eng. J.* **2022**, *450*, 137893. DOI
71. Che, X.; Zhang, W.; Long, L.; et al. Mildly peeling off and encapsulating large MXene nanosheets with rigid biologic fibrils for synchronization of solar evaporation and energy harvest. *ACS. Nano.* **2022**, *16*, 8881-90. DOI
72. Peng, H.; Wang, D.; Fu, S. Unidirectionally driving nanofluidic transportation via an asymmetric textile pump for simultaneous salt-resistant solar desalination and drenching-induced power generation. *ACS. Appl. Mater. Interfaces.* **2021**, *13*, 38405-15. DOI
73. Park, H.; Choi, G.; Yoon, S.; et al. MXene-enhanced ionovoltaic effect by evaporation and water infiltration in semiconductor nanochannels. *ACS. Nano.* **2024**, *18*, 13130-40. DOI
74. Chen, Y.; He, J.; Ye, C.; Tang, S. Achieving ultrahigh voltage over 100 V and remarkable freshwater harvesting based on thermodiffusion enhanced hydrovoltaic generator. *Adv. Energy. Mater.* **2024**, *14*, 2400529. DOI
75. Zhang, Z.; Wen, L.; Jiang, L. Nanofluidics for osmotic energy conversion. *Nat. Rev. Mater.* **2021**, *6*, 622-39. DOI
76. Hong, S.; Ming, F.; Shi, Y.; et al. Two-dimensional $Ti_3C_2T_x$ MXene membranes as nanofluidic osmotic power generators. *ACS. Nano.* **2019**, *13*, 8917-25. DOI
77. Chang, L.; Zhang, T.; Wang, F.; et al. Cation-selective $Mo_2TiC_2T_x$ MXene membrane for osmotic energy harvesting. *2D. Mater.* **2023**, *10*, 014009. DOI
78. Qin, H.; Wu, H.; Zeng, S.; et al. Harvesting osmotic energy from proton gradients enabled by two-dimensional $Ti_3C_2T_x$ MXene membranes. *Adv. Membr.* **2022**, *2*, 100046. DOI
79. Dong, Q.; Liu, J.; Wang, Y.; He, J.; Zhai, J.; Fan, X. Ultrathin H-MXM as an "ion freeway" for high-performance osmotic energy conversion. *Small. Methods.* **2024**, *8*, e2301558. DOI
80. Hong, S.; El-Demellawi, J. K.; Lei, Y.; et al. Porous $Ti_3C_2T_x$ MXene membranes for highly efficient salinity gradient energy harvesting. *ACS. Nano.* **2022**, *16*, 792-800. DOI PubMed PMC
81. Wang, S.; Wang, Z.; Fan, Y.; Meng, X.; Wang, F.; Yang, N. Toward explicit anion transport nanochannels for osmotic power energy using positive charged MXene membrane via amination strategy. *J. Membr. Sci.* **2023**, *668*, 121203. DOI
82. Ding, L.; Xiao, D.; Lu, Z.; et al. Oppositely charged $Ti_3C_2T_x$ MXene membranes with 2D nanofluidic channels for osmotic energy harvesting. *Angew. Chem. Int. Ed.* **2020**, *59*, 8720-6. DOI
83. Hashemifar, F.; Esfandiar, A. Oppositely charged MXene fibers as a highly efficient osmotic power generator from sea and river water. *J. Mater. Chem. A.* **2022**, *10*, 24915-26. DOI
84. Ding, L.; Zheng, M.; Xiao, D.; et al. Bioinspired $Ti_3C_2T_x$ MXene-based ionic diode membrane for high-efficient osmotic energy conversion. *Angew. Chem. Int. Ed.* **2022**, *61*, e202206152. DOI

85. Chen, Y.; Fang, M.; Ding, S.; et al. Bioinspired ultrastable MXene/PEDOT:PSS layered membrane for effective salinity gradient energy harvesting from organic solvents. *ACS. Appl. Mater. Interfaces.* **2022**, *14*, 23527-35. DOI
86. Jang, J.; Kang, Y.; Kim, K.; et al. Concrete-structured Nafion@MXene/Cellulose acetate cation exchange membrane for reverse electrodialysis. *J. Membr. Sci.* **2022**, *646*, 120239. DOI
87. Nazif, A.; Saljoughi, E.; Mousavi, S. M.; Karkhanechi, H. Embedding MXene nanosheets into cation exchange membranes to enhance power generation by reverse electrodialysis. *Desalination* **2023**, *566*, 116926. DOI
88. Ren, Z.; Zhang, Q.; Yin, J.; et al. Enhancing osmotic energy harvesting through supramolecular design of oxygen-functionalized MXene with biomimetic ion channels. *Adv. Funct. Mater.* **2024**, *34*, 2404410. DOI
89. Lin, X.; Liu, P.; Xin, W.; et al. Heterogeneous MXene/PS-b-P2VP nanofluidic membranes with controllable ion transport for osmotic energy conversion. *Adv. Funct. Mater.* **2021**, *31*, 2105013. DOI
90. Duan, R.; Zhou, J.; Ma, X.; et al. High strength MXene/PBONF heterogeneous membrane with excellent ion selectivity for efficient osmotic energy conversion. *Nano. Lett.* **2023**, *23*, 11043-50. DOI
91. Yuan, Z.; Zhou, B.; Yuan, K.; et al. High-aligned oppositely-charged nanocellulose/MXene aerogel membranes through synergy of directional freeze-casting and structural densification for osmotic-energy harvesting. *Nano. Energy.* **2024**, *124*, 109450. DOI
92. Sun, Z.; Ahmad, M.; Gao, Z.; et al. Highly ionic conductive and mechanically strong MXene/CNF membranes for osmotic energy conversion. *Sustain. Energy. Fuels.* **2022**, *6*, 299-308. DOI
93. Zhai, R.; Jiang, L.; Chen, Z.; et al. Kelp nanofiber-based composite membranes for highly efficient osmotic energy conversion. *Adv. Funct. Mater.* **2024**, *34*, 2313914. DOI
94. Zhang, Z.; Yang, S.; Zhang, P.; Zhang, J.; Chen, G.; Feng, X. Mechanically strong MXene/Kevlar nanofiber composite membranes as high-performance nanofluidic osmotic power generators. *Nat. Commun.* **2019**, *10*, 2920. DOI PubMed PMC
95. Rao, J.; Lv, Z.; Yan, X.; et al. Nacre-inspired mechanically robust films for osmotic energy conversion. *Adv. Funct. Mater.* **2024**, *34*, 2309869. DOI
96. Song, G.; Zhan, Y.; Hu, Y.; et al. Paper-mill waste reinforced nanofluidic membrane as high-performance osmotic energy generators. *Adv. Funct. Mater.* **2023**, *33*, 2214044. DOI
97. Wang, B.; Li, J.; Wu, Z.; et al. Salinity power generation based biocompatible bacterial cellulose/MXene membrane for biological power source. *Nano. Energy.* **2022**, *102*, 107702. DOI
98. Li, X.; He, J.; Lu, B.; Zhai, J. Soil-inspired multi-stage heterogeneous nanochannel membranes for enhanced osmotic energy conversion. *Chem. Eng. J.* **2024**, *493*, 152375. DOI
99. Liu, P.; Zhou, T.; Yang, L.; et al. Synergy of light and acid-base reaction in energy conversion based on cellulose nanofiber intercalated titanium carbide composite nanofluidics. *Energy. Environ. Sci.* **2021**, *14*, 4400-9. DOI
100. Xu, Y.; Zhang, K.; Chen, S.; et al. Two-dimensional lamellar MXene/three-dimensional network bacterial nanocellulose nanofiber composite Janus membranes as nanofluidic osmotic power generators. *Electrochim. Acta.* **2022**, *412*, 140162. DOI
101. Wang, L.; Feng, Y.; Zhou, Y.; et al. Photo-induced active ion transport-assisted efficient ionic power harvesting from bioinspired Janus dual-field heterostructures. *Adv. Funct. Mater.* **2024**, *34*, 2314165. DOI
102. Yang, G.; Qian, Y.; Wang, L.; et al. Advanced Janus membrane (MXene/CoAl-LDH) for efficient asymmetric ion transport and nanofluidic energy harvesting. *Nano. Energy.* **2023**, *118*, 108972. DOI
103. Wang, F.; Wang, Z.; Meng, X.; et al. Advancing osmotic power generation using bioinspired MXene-based membrane via maze breaking. *J. Membr. Sci.* **2023**, *686*, 121975. DOI
104. Wang, F.; Wang, Z.; Wang, S.; et al. Mechanically intensified and stabilized MXene membranes via the combination of graphene oxide for highly efficient osmotic power production. *J. Membr. Sci.* **2022**, *647*, 120280. DOI
105. Yang, G.; Liu, D.; Chen, C.; et al. Stable $Ti_3C_2T_x$ MXene-boron nitride membranes with low internal resistance for enhanced salinity gradient energy harvesting. *ACS. Nano.* **2021**, *15*, 6594-603. DOI
106. Gao, H.; Chen, W.; Xu, C.; Liu, S.; Tong, X.; Chen, Y. Two-dimensional $Ti_3C_2T_x$ MXene/GO hybrid membranes for highly efficient osmotic power generation. *Environ. Sci. Technol.* **2020**, *54*, 2931-40. DOI
107. Van Nguyen, T.; Tekalgne, M.; Van Le, Q.; Van Tran, C.; Ahn, S. H.; Kim, S. Y. Recent progress and strategies of non-noble metal electrocatalysts based on MoS_2/MOF for the hydrogen evolution reaction in water electrolysis: an overview. *Microstructures* **2024**, *4*, 2024046. DOI
108. Huang, R.; Wang, Y.; You, D.; et al. MOF and its derivative materials modified lithium-sulfur battery separator: a new means to improve performance. *Rare. Met.* **2024**, *43*, 2418-43. DOI
109. Su, Y.; Yuan, G.; Hu, J.; et al. Recent progress in strategies for preparation of metal-organic frameworks and their hybrids with different dimensions. *Chem. Synth.* **2023**, *3*, 1. DOI
110. Mane, R. S.; Mane, S.; Somkuwar, V.; Thombre, N. V.; Patwardhan, A. V.; Jha, N. A novel hierarchically hybrid structure of MXene and bi-ligand ZIF-67 based trifunctional electrocatalyst for zinc-air battery and water splitting. *Battery. Energy.* **2023**, *2*, 20230019. DOI
111. Zhou, J.; Hao, J.; Wu, R.; et al. Maximizing ion permselectivity in MXene/MOF nanofluidic membranes for high-efficient blue energy generation. *Adv. Funct. Mater.* **2022**, *32*, 2209767. DOI
112. Yao, B.; Fang, Z.; Hu, Y.; Ye, Z.; Peng, X. Enhanced osmotic power generation through anodic electrodeposited MOFs@MXene heterostructured nanochannels. *J. Membr. Sci.* **2024**, *709*, 123116. DOI
113. Yang, L.; Cao, L. N.; Li, S.; et al. MOFs/MXene nano-hierarchical porous structures for efficient ion dynamics. *Nano. Energy.* **2024**,

129, 110076. DOI

114. Lin, W.; Huang, T.; Bai, C.; et al. Novel ultrastable 2D MOF/MXene nanofluidic membrane with ultralow resistance for highly efficient osmotic power harvesting. *Nano. Energy.* **2024**, *128*, 109924. DOI
115. Yang, Y.; Wang, D.; Liao, W.; et al. Arch-bridge photothermal fabric with efficient warp-direction water paths for continuous solar desalination. *Adv. Fiber. Mater.* **2024**, *6*, 1026-36. DOI
116. Chang, J.; Pang, B.; Zhang, H.; Pang, K.; Zhang, M.; Yuan, J. MXene/Cellulose composite cloth for integrated functions (if-Cloth) in personal heating and steam generation. *Adv. Fiber. Mater.* **2024**, *6*, 252-63. DOI PubMed PMC
117. Liu, P.; Zhou, T.; Teng, Y.; et al. Light-induced heat driving active ion transport based on 2D MXene nanofluids for enhancing osmotic energy conversion. *CCS. Chem.* **2021**, *3*, 1325-35. DOI
118. Xia, J.; Gao, H.; Pan, S.; et al. Light-augmented multi-ion interaction in MXene membrane for simultaneous water treatment and osmotic power generation. *ACS. Nano.* **2023**, *17*, 25269-78. DOI
119. Yin, J.; Li, X.; Yu, J.; Zhang, Z.; Zhou, J.; Guo, W. Generating electricity by moving a droplet of ionic liquid along graphene. *Nat. Nanotechnol.* **2014**, *9*, 378-83. DOI
120. Bai, Y.; Chen, C.; Liu, X.; Gao, J.; Sui, K. Power generation via sliding ionic droplets on nanolayered MXene films. *ACS. Appl. Nano. Mater.* **2022**, *5*, 4597-602. DOI
121. Lao, J.; Wu, S.; Gao, J.; Dong, A.; Li, G.; Luo, J. Electricity generation based on a photothermally driven $Ti_3C_2T_x$ MXene nanofluidic water pump. *Nano. Energy.* **2020**, *70*, 104481. DOI
122. Si, P.; Li, M.; Wang, X.; et al. Origin of enhanced electricity generation on Magnéli phase titanium suboxide nanocrystal films. *ACS. Appl. Energy. Mater.* **2021**, *4*, 10877-85. DOI
123. Li, S.; Zhao, K.; Zan, G.; et al. A biodegradable silk-based energy-generating skin with dual-mode tactile perception. *Device* **2025**, *3*, 100561. DOI
124. Wu, H.; Zheng, H.; Qin, X.; et al. Drinking-bird-enabled triboelectric hydrovoltaic generator. *Device* **2024**, *2*, 100318. DOI
125. Zhang, X.; Liang, J.; Ahmad, K.; Almutairi, Z.; Wan, C. Moisture-driven fabric-based generator for powering wearable electronics. *Device* **2024**, *2*, 100316. DOI
126. Yan, H.; Qi, R.; Liu, Z.; Wang, H.; Dong, C.; Zhang, L. Unlocking the potential of hydrogel-electrode electrical double layer for high-performance moisture-enabled electric generators. *Device* **2025**, *3*, 100568. DOI
127. Benedetto, G. A smart fabric nanogenerator combines energy sources to power devices. *Device* **2023**, *1*, 100177. DOI
128. Zou, R.; Chen, H.; Pan, H.; et al. Self-powered and self-sensing wearable devices from a comfort perspective. *Device* **2024**, *2*, 100466. DOI
129. Liu, C.; Wang, F.; Du, X. Self-powered electrostatic tweezer for adaptive object manipulation. *Device* **2024**, *2*, 100465. DOI
130. Yin, J.; Kashyap, V.; Wang, S.; Xiao, X.; Tat, T.; Chen, J. Self-powered eye-computer interaction via a triboelectric nanogenerator. *Device* **2024**, *2*, 100252. DOI
131. Wang, T.; Li, C.; Gao, Z.; et al. Triboelectric encoders for accurate and durable wearable motion sensing. *Device* **2024**, *2*, 100525. DOI
132. Li, S.; Liu, A.; Qiu, W.; et al. An all-protein multisensory highly bionic skin. *ACS. Nano.* **2024**, *18*, 4579-89. DOI
133. Wang, Y.; Qu, K.; Li, S.; et al. Fully degradable, highly elastomeric and adhesive silk fibroin electronic skin for microdynamic pressure monitoring. *Chem. Eng. J.* **2023**, *469*, 143920. DOI
134. Li, S. Y.; Liu, J. R.; Wen, H.; Liu, X. Y.; Guo, W. X. Recent advances in silk-based wearable sensors. *Acta. Phys. Sin.* **2020**, *69*, 178703. DOI
135. Li, S.; Liu, G.; Wen, H.; et al. A skin-like pressure- and vibration-sensitive tactile sensor based on polyacrylamide/silk fibroin elastomer. *Adv. Funct. Mater.* **2022**, *32*, 2111747. DOI